J. Fluid Mech. (2011), *vol.* 666, *pp.* 204–253.
doi:10.1017/S0022112010004143

Weakly nonlinear theory of shear-banding instability in a granular plane Couette flow: analytical solution, comparison with numerics and bifurcation

PRIYANKA SHUKLA AND MEHEBOOB ALAM†

Engineering Mechanics Unit, Jawaharlal Nehru Centre for Advanced Scientific Research, Jakkur PO, Bengaluru 560064, India

(Received 18 January 2010; revised 26 July 2010; accepted 30 July 2010; first published online 16 November 2010)

A weakly nonlinear theory, in terms of the well-known Landau equation, has been developed to describe the nonlinear saturation of the shear-banding instability in a rapid granular plane Couette flow using the amplitude expansion method. The nonlinear modes are found to follow certain symmetries of the base flow and the fundamental mode, which helped to identify analytical solutions for the base-flow distortion and the second harmonic, leading to an exact calculation of the first Landau coefficient. The present analytical solutions are used to validate a spectral-based numerical method for the nonlinear stability calculation. The regimes of supercritical and subcritical bifurcations for the shear-banding instability have been identified, leading to the prediction that the lower branch of the neutral stability contour in the (H, ϕ^0)-plane, where H is the scaled Couette gap (the ratio between the Couette gap and the particle diameter) and ϕ^0 is the mean density or the volume fraction of particles, is subcritically unstable. The predicted finite-amplitude solutions represent shear localization and density segregation along the gradient direction. Our analysis suggests that there is a sequence of transitions among three types of pitchfork bifurcations with increasing mean density: from (i) the bifurcation from infinity in the Boltzmann limit to (ii) subcritical bifurcation at moderate densities to (iii) supercritical bifurcation at larger densities to (iv) subcritical bifurcation in the dense limit and finally again to (v) supercritical bifurcation near the close packing density. It has been shown that the appearance of subcritical bifurcation in the dense limit depends on the choice of the contact radial distribution function and the constitutive relations. The scalings of the first Landau coefficient, the equilibrium amplitude and the phase diagram, in terms of mode number and inelasticity, have been demonstrated. The granular plane Couette flow serves as a paradigm that supports all three possible types of pitchfork bifurcations, with the mean density (ϕ^0) being the single control parameter that dictates the nature of the bifurcation. The predicted bifurcation scenario for the shear-band formation is in qualitative agreement with particle dynamics simulations and the experiment in the rapid shear regime of the granular plane Couette flow.

Key words: bifurcation, granular media, nonlinear instability

† Email address for correspondence: meheboob@jncasr.ac.in

1. Introduction

The lack of a unified theory for granular materials, a collection of macroscopic 'dissipative' particles, for different flow regimes of dilute to dense flows is largely responsible for a poor understanding of its dynamical behaviour and the related pattern formation scenario. Over the last 10 years, there has been a surge in research activity to unveil the pattern formation scenario in various types of granular flows (such as Couette flow, Poiseuille flow, vibrated bed and inclined chute flow), especially in the rapid flow regime (Goldhirsch 2003; Aranson & Tsimring 2006). The granular plane Couette flow is the prototype problem that supports various types of stationary and travelling wave instabilities as predicted from the linear stability theory (Alam & Nott 1998) – the related patterns have subsequently been verified in particle simulations of the plane Couette flow (Conway & Glasser 2004). Another interesting pattern that appears in a flowing granular material is the 'shear-band': when a granular material is sheared in shear-cell experiments (Savage & Sayed 1984; Mueth *et al.* 2000; Schall & van Hecke 2010), shearing remains confined to a narrow localized zone (i.e. a 'shear-band' where the shear rate is non-zero) near the walls and the rest of the material remains almost unsheared (i.e. a 'plug' where the shear rate is close to zero). Such a shear-banding phenomenon, where the shear rate is non-uniform along the gradient direction in a plane shear set-up, seems to be generic in wall-driven flows and occurs in a variety of sheared complex fluids: colloidal suspensions (Hoffman 1972), worm-like micelles (Berret, Porte & Decruppe 1997), lyotropic liquid crystals (Bonn *et al.* 1998), suspensions of rod-like viruses (Lettinga & Dhont 2004) and liquid–liquid biphasic systems (Caserta, Simeon & Guido 2008). One possible origin of shear-banding is bulk instability of the complex fluid (Greco & Ball 1997; Alam & Nott 1998), the signature of which is implicated in the 'non-monotonic' variation in certain constitutive/rheological field (stress or dynamic friction) with some hydrodynamic field (shear rate or density) – this is reminiscent of 'phase-transition' in driven systems; see Olmsted (2008) for a review on shear-banding phenomena. Such shear-banding, wherein the flow undergoes an ordering transition into alternate layers of dense and dilute regions of low and high shear rates, respectively, aligned along the gradient direction (i.e. the density bands are parallel to the flow direction), has also been realized in the molecular dynamics simulations of granular Couette flow (Tan 1995; Alam & Luding 2003; Khain 2007) for a range of densities from dilute to dense flows (without gravity) in the rapid flow regime. A possible theoretical description of shear-banding phenomena in terms of order-parameter equations is the focus of this paper.

The Ginzburg–Landau-type order-parameter equations have been widely used to study the bifurcation scenario, nonlinear waves and patterns in fluid mechanics (Newell, Passot & Lega 1993; Manneville 1990; Cross & Hohenberg 1993). In condensed matter physics, the complex Ginzburg–Landau equation has been used to obtain a qualitative (and sometimes quantitative) understanding of a host of phenomena, namely phase transitions, superconductivity, superfluidity, liquid crystals, vortex glass and defect turbulence (Cross & Hohenberg 1993; Aranson & Kramer 2002). Moving from traditional fluid mechanics (Newell *et al.* 1993) to the 'dissipative' granular fluid, it is appropriate to pose the question: can Ginzburg–Landau-type order-parameter theories be used to probe the pattern formation scenario in granular flows? In the context of granular fluid, Tsimring & Aranson (1997) first postulated a complex Ginzburg–Landau equation which is coupled to mass and momentum balance equations. This set of equations, called order-parameter theory, was then shown to reproduce the complete phase diagram of

patterns (e.g. squares, stripes, hexagons and oscillons) in a shallow vibrated bed (Umbanhower, Mello & Swinney 1996) – this underscores the success of their order-parameter theory. Subsequently, they have used this order-parameter theory to probe the pattern formation scenario in a variety of flowing granular systems; see the review by Aranson & Tsimring (2006). Despite its success, note that the foundation of this order-parameter theory of granular fluid is empirical since the related order-parameter equation has been postulated with fitting parameters (that vary from one flow to another), which must be obtained from simulation/experiment.

Against this background, a more pertinent question in this context is as follows: is it possible to derive the relevant order-parameter equation of granular flows to describe pattern formation from first principles? Over the last two decades, the well-studied granular hydrodynamic models have been derived from the dense gas kinetic theory (Lun *et al.* 1984; Sela & Goldhirsch 1998; Brey, Santos & Dufty 1998; Garzo & Dufty 1999; Brilliantov & Pöschel 2004). Such hydrodynamic models have been reasonably successful in describing both the rheology and the flow dynamics of granular materials in a variety of flow configurations in the rapid shear regime (see Goldhirsch 2003 for a review). Starting with such continuum models, we could follow the route of nonlinear stability theory (Stuart 1960; Watson 1960; Reynolds & Potter 1967; Busse 1978; Newell *et al.* 1993) to derive the relevant order-parameter equation for describing the bifurcation scenario and patterns in granular flows. This is precisely what we have recently done to probe the shear-banding phenomenon in the granular plane Couette flow via an order-parameter equation: we used the centre-manifold reduction technique (Carr 1981) to derive the Landau equation (Shukla & Alam 2009).

In the present paper, we develop a weakly nonlinear stability theory for the same 'shear-banding' phenomena using a different method: the amplitude expansion method of Stuart (1960) and Watson (1960). This is an indirect method to arrive at the Landau equation and complements our previous effort (Shukla & Alam 2009) that used a direct method of centre-manifold reduction (Carr 1981). It is important to understand the difference between the present formalism of amplitude expansion method and the centre-manifold reduction. The Landau equation is postulated to hold in the amplitude expansion method, and the Landau coefficients are determined from the solvability condition of certain inhomogeneous differential equations at higher order (cubic, quintic, etc.) in perturbation amplitudes. This is in contrast to the direct method of centre-manifold reduction (Shukla & Alam 2009) wherein the Landau equation is derived from the evolution equation of the slow mode via its inner product with the adjoint linear eigenfunction, and the expressions for Landau coefficients appear in the resultant Landau equation as the coefficients of terms of appropriate order in perturbation amplitudes. The underlying subtle differences between the two methods will be made clear in § 4. One of the goals of the present paper is to show that both the direct and indirect methods of nonlinear stability lead to the same order-parameter equation, with the same expression for the first Landau coefficient for the present problem of granular shear flow. This, in turn, establishes an equivalence between these two seemingly different methods of nonlinear stability for granular shear flows (which are much more complicated than incompressible shear flows of Newtonian fluids). Put differently, it should be mentioned that the weakly nonlinear stability theories for compressible Newtonian fluids (e.g. air) are very scarce and we have not found any prior work, for example, on the compressible plane Couette flow (see Malik, Dey & Alam 2008 and references therein).

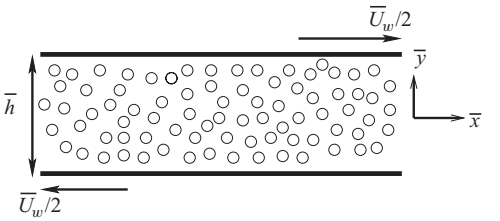

FIGURE 1. Schematic diagram of the plane shear flow between parallel plates. The upper plate moves with the velocity $\overline{U}_w/2$ along the positive $\overline{x}$-direction and the lower plate moves with the same speed in the opposite direction.

The present analysis can also be adapted to probe the nonlinear stability of compressible shear flows.

This paper is organized as follows. The continuum equations and boundary conditions are presented in § 2. The nonlinear perturbation equations and the related linear adjoint system are formulated in § 3. The methodology of the amplitude expansion technique is discussed and compared with the centre-manifold reduction technique in detail in § 4. We show that the first Landau coefficients (which determine the type of bifurcation that the flow is supposed to undergo at the onset of pattern formation) obtained from both these methods are identical. The symmetries of the linear and nonlinear modes are discussed in § 5. A spectral-based numerical scheme has been developed to solve the related nonlinear stability problems as detailed in § 6. The symmetries of the underlying nonlinear modes have helped us to identify analytical solutions for the second harmonic, the base-flow distortion and the distortion of the fundamental mode, leading to an exact calculation of the first Landau coefficient – these analytical solutions and their comparison with numerical solutions are detailed in §§ 7.1–7.3. The comparison between numerical and analytical solutions validates our spectral-based numerical scheme, which is another outcome of this paper. The predictions of our analytical order-parameter theory are discussed in § 8.1 (linear shear-banding instability), § 8.2 (equilibrium amplitude and the nature of bifurcation), § 8.3 (phase diagram for nonlinear stability), § 8.4 (finite amplitude solutions) and § 8.5 (scaling of the first Landau coefficient, equilibrium amplitude and phase diagram). The influence of different forms of the contact radial distribution function and the constitutive relations on our predictions is discussed in §§ 9.1 and 9.2, respectively, along with a summary of all possible bifurcation scenarios for the nonlinear shear-banding instability in the granular plane Couette flow in § 9.3. A qualitative comparison of our predictions on the bifurcation scenario with particle simulations and experiment is given in § 9.4. We summarize the major findings of this paper and suggest future extensions of the present order-parameter theory in § 10.

2. Plane Couette flow: continuum equations and boundary conditions

Consider a flow of granular particles between two infinite parallel plates at $\overline{y} = \pm\overline{h}/2$, where $\overline{h}$ is the gap between the plates as shown in figure 1; both the plates are moving in the opposite direction along the $\overline{x}$-direction with the velocity $\overline{U}_w/2$. Here, the overbar denotes a dimensional quantity. The physical state of the particles of the granular system under study is that the particles are monodisperse, smooth, spherical and inelastic with the particle diameter $\overline{d}$ and the coefficient of restitution e. Here $\overline{\varrho} = \overline{m}\overline{n} = \overline{\rho}\phi$ is the mass density, $\overline{m}$ is the particle mass, $\overline{n}$ is the

number density of particles, $\overline{\rho}$ is the material density (mass density of individual particles), and ϕ is the volume fraction of the particles or the solid fraction; $\overline{\boldsymbol{u}} = (\overline{u}, \overline{v})$ is the bulk (coarse-grained) velocity and $\overline{T}$ is the granular temperature (i.e. fluctuation kinetic energy of particles).

The boundary conditions are chosen to be no-slip velocity and zero heat flux: $\overline{u}(\overline{y} = \pm\overline{h}/2) = \pm\overline{U}_w/2$, $\overline{v}(\overline{y} = \pm\overline{h}/2) = 0$ and $\mathrm{d}\overline{T}/\mathrm{d}\overline{y}(\overline{y} = \pm\overline{h}/2) = 0$. For the purposes of non-dimensionalization, we use the reference length, velocity and time scales as $\overline{h}$, $\overline{U}_w$ and $\overline{h}/\overline{U}_w$, respectively, and the material density $\overline{\rho}$ is used to non-dimensionalize the mass density $\overline{\varrho}$ wherever it appears; see Alam & Nott (1998) and Alam, Shukla & Luding (2008) for related details. In the following, all 'unbarred' quantities are dimensionless.

2.1. *Streamwise-independent equations*

The full tensorial form of balance equations and the constitutive relations for the stress tensor, the granular heat flux and the rate of collisional dissipation can be found in our previous paper (Alam *et al.* 2008). Since the focus of this paper is on the shear-banding instability, which originates from a specific form of perturbations having no variation along the streamwise direction (x), here we start with the simplified form of balance equations that do not depend on the streamwise coordinate. In the dimensionless form, the streamwise-independent ($\partial/\partial x(\cdot) = 0$) balance equations for mass, momentum and granular energy, respectively, are

$$\frac{\partial \phi}{\partial t} + \phi\frac{\partial v}{\partial y} + v\frac{\partial \phi}{\partial y} = 0, \tag{2.1}$$

$$\phi\left[\frac{\partial}{\partial t} + v\frac{\partial}{\partial y}\right]u = \frac{1}{H^2}\frac{\partial}{\partial y}\left(\mu\frac{\partial u}{\partial y}\right), \tag{2.2}$$

$$\phi\left[\frac{\partial}{\partial t} + v\frac{\partial}{\partial y}\right]v = \frac{1}{H^2}\left[-\frac{\partial p}{\partial y} + \frac{\partial}{\partial y}\left(2\mu\frac{\partial v}{\partial y} + \lambda\frac{\partial v}{\partial y}\right)\right], \tag{2.3}$$

$$\begin{aligned}\frac{\dim}{2}\phi\left[\frac{\partial}{\partial t} + v\frac{\partial}{\partial y}\right]T = {} & \frac{1}{H^2}\frac{\partial}{\partial y}\left(\kappa\frac{\partial T}{\partial y}\right) - p\frac{\partial v}{\partial y} \\ & + 2\mu\left[\left(\frac{\partial v}{\partial y}\right)^2 + \frac{1}{2}\left(\frac{\partial u}{\partial y}\right)^2 + \frac{\lambda}{2\mu}\left(\frac{\partial v}{\partial y}\right)^2\right] - \mathscr{D}.\end{aligned} \tag{2.4}$$

Here, $H = \overline{h}/\overline{d}$ is the ratio between the Couette gap ($\overline{h}$) and the particle diameter ($\overline{d}$), called the 'scaled Couette gap', which can equivalently be thought of as the inverse of the dimensionless particle diameter i.e. $H = (\overline{d}/\overline{h})^{-1}$; 'dim' refers to the dimensionality of the problem (dim = 3 for spheres and 2 for disks). The dimensionless transport coefficients are

$$\left.\begin{aligned} p(\phi, T) &= f_1(\phi)T && \text{(pressure)},\\ \mu(\phi, T) &= f_2(\phi)\sqrt{T} && \text{(shear viscosity)},\\ \zeta(\phi, T) &= f_3(\phi)\sqrt{T} && \text{(bulk viscosity)},\\ \kappa(\phi, T) &= f_4(\phi)\sqrt{T} && \text{(granular thermal conductivity)},\\ \mathscr{D}(\phi, T) &= f_5(\phi, e)T^{3/2} && \text{(collisional dissipation rate)},\\ \lambda(\phi, T) &= \zeta - \frac{2}{\dim}\mu, \end{aligned}\right\} \tag{2.5}$$

where $f_i(.)$ values are dimensionless functions of the solid fraction:

$$\left.\begin{aligned} f_1(\phi) &= \phi(1+4\phi\chi), \\ f_2(\phi) &= \frac{5\sqrt{\pi}}{96\chi}\left(1+\frac{8}{5}\phi\chi\right)^2+\frac{8}{5\sqrt{\pi}}\phi^2\chi, \\ f_3(\phi) &= \frac{8}{3\sqrt{\pi}}\phi^2\chi, \\ f_4(\phi) &= \frac{25\sqrt{\pi}}{128\chi}\left(1+\frac{12}{5}\phi\chi\right)^2+\frac{4}{\sqrt{\pi}}\phi^2\chi, \\ f_5(\phi,e) &= \frac{12}{\sqrt{\pi}}(1-e^2)\phi^2\chi. \end{aligned}\right\} \tag{2.6}$$

The contact radial distribution function, $\chi(\phi)$, is

$$\chi(\phi) = \frac{1}{1-(\phi/\phi_m)^{1/3}}, \tag{2.7}$$

where ϕ_m corresponds to the maximum solid fraction at a random close packing which is taken to be 0.65 in this work. All results, up to § 8, are presented for (2.7), but the effect of other choices of $\chi(\phi)$ on our predictions is discussed in § 9.1. Also, the effect of different forms of f_i values in (2.6) that are valid for hard disks (dim = 2) is discussed in § 9.2.

It may be noted that we have chosen a Navier–Stokes-order constitutive model (Lun *et al.* 1984), which has been used by a number of authors (Alam & Nott 1998; Forterre & Pouliquen 2002; Alam *et al.* 2005; Khain 2007) to probe the stability of various types of granular shear flows. In the expression for the collisional dissipation $\mathscr{D}$ (which is proportional to $f_5(\phi, e)$ as in (2.6)), some authors (e.g. Garzo & Dufty 1999) have found an additional contribution proportional to $\nabla \cdot \boldsymbol{u}$, which appears as a dense gas correction. We have checked that this additional term does not affect the onset of linear shear-banding instability and it is hence omitted in the present work. We have also neglected a 'Dufour-like' term ($\sim\nabla\phi$) in the expression for the granular heat flux (see, for example, Lun *et al.* 1984; Sela & Goldhirsch 1998; Garzo & Dufty 1999) – even though this is a Navier–Stokes-order term, i.e. of the order of the Knudsen number (Kn), it appears at $O(\epsilon Kn)$, where $\epsilon = (1-e^2)$ is the inelasticity. However, it can be easily verified that the shear rate ($\sim Kn$) and the inelasticity cannot be separated from each other ($Kn \sim \sqrt{\epsilon}$) in a uniform shear flow and, therefore, the above 'Dufour-like' term is likely to be of higher order in terms of the Knudsen number. In any case, the effect of this additional term on the stability of the uniform shear flow, along with the effects of spin fields and tangential restitution, was checked by Gayen & Alam (2006), who showed that this term does not introduce any new instability in the plane shear flow.

Note that Gayen & Alam (2006) used more general expressions for f_1–f_4 in (2.6), which also depend on the restitution coefficient e, having a larger range of validity in terms of e; for example, the correct expression for f_1 for inelastic particles is $f_1(\phi, e) = \phi(1+2(1+e)\phi\chi)$, with similar expressions for f_2–f_4. Even with such an elaborate restitution-coefficient-dependent constitutive model, they reported no new instability in plane shear flow. Since the present nonlinear analysis is a finite-amplitude saturation of the underling linearly unstable mode, our contention is that a more complex restitution-coefficient-dependent constitutive model would not qualitatively alter our predictions on 'nonlinear' shear-banding instability.

The Navier–Stokes-level constitutive models are strictly valid in the quasi-elastic limit ($e \sim 1$) since certain non-Newtonian effects, such as the normal stress differences (Sela & Goldhirsch 1998; Alam & Luding 2003, 2005; Chikkadi & Alam 2009), become prominent at smaller values of the restitution coefficient (i.e. at larger dissipation levels). Such effects can only be incorporated using Burnett- or super-Burnett order constitutive models (Sela & Goldhirsch 1998), which we do not consider here. It should, however, be noted that the nonlinear analysis presented in §§ 3 and 4 can also be easily adapted to non-Newtonian constitutive models and, therefore, our nonlinear order-parameter theory, as described in §§ 3 and 4, is of general import.

The boundary conditions in the dimensionless form are

$$u = \pm\frac{1}{2}, \quad v = 0, \quad \frac{\mathrm{d}T}{\mathrm{d}y} = 0 \quad \text{at} \quad y = \pm 1/2, \tag{2.8}$$

which correspond to zero-slip, zero-penetration and zero heat-flux, respectively. More general forms of the boundary condition with non-zero slip velocity and/or non-adiabatic ($\mathrm{d}T/\mathrm{d}y \neq 0$) walls can be incorporated into the nonlinear stability theory, but the resulting nonlinear analysis (especially the adjoint problem and the higher harmonics) becomes very complicated, which we do not discuss in this paper. As rightly pointed out by one reviewer, the walls can act as sources or sinks of granular (fluctuation) energy, which might affect the nonlinear saturation of the shear-banding instability, thereby modifying the structure and the spatial position of shear-bands within the Couette cell. The effect of such slip boundary conditions with non-adiabatic walls on the 'linear' shear-banding instability has been discussed by Alam & Nott (1998), to which we refer the readers for related details. In this paper, as a first step towards developing an order-parameter theory, we restrict ourselves to simpler boundary conditions (2.8) that admit analytical solutions even for the nonlinear problem and the related bifurcation scenario remains perfect (Alam 2005; Alam *et al.* 2005), leaving aside the related imperfect problem with realistic boundary conditions (Chikkadi & Alam 2009) to a future work.

2.2. *Steady plane Couette flow: base state*

The stability of the flow which we want to study is the steady, fully developed, two-dimensional flow between two infinite parallel moving plates. Under these assumptions, we can write the base state solution as

$$\phi = \phi^0(y), \quad \boldsymbol{u} = (u^0(y), 0), \quad T = T^0(y). \tag{2.9}$$

With no-slip and adiabatic boundary conditions (2.8), the resulting base flow equations admit the following solution of uniform shear with constant density and granular temperature:

$$u^0(y) = y, \quad v^0 = 0, \quad \phi^0 = \text{constant}, \quad T^0(\phi^0) = \text{constant} = \frac{f_2(\phi^0)}{f_5(\phi^0, e)}, \tag{2.10}$$

where $f_2(\phi^0)$ and $f_5(\phi^0, e)$ are given by (2.6). Note that the pressure (p^0) and the shear stress [$\mu^0(\mathrm{d}u^0/\mathrm{d}y)$] are also constants for the steady plane Couette flow. In the following discussion, we use density or solid fraction or volume fraction to refer to the same quantity ϕ.

3. Nonlinear disturbance equations and linear adjoint system

The stability of the basic flow is examined by decomposing all the flow variables and transport coefficients into a base flow part and a finite-amplitude perturbation:

$\phi(y,t)=\phi^0(y)+\phi'(y,t)$, where the superscript 0 denotes the base state and the prime denotes its perturbation. The transport coefficients are analytic functions of density and temperature, and hence can be written as a Taylor series around the base state, i.e.

$$p(\phi,T)=p^0+p^0_\phi\phi'+p^0_T T'+\frac{1}{2!}\left(p^0_{\phi\phi}\phi'^2+p^0_{\phi T}\phi'T'+p^0_{TT}T'^2+p^0_{T\phi}T'\phi'\right)+\cdots, \tag{3.1}$$

where the subscripts denote the respective partial derivatives, and the superscript 0 implies that the quantity is to be evaluated at the base flow conditions. Inserting the Taylor series expansions of all hydrodynamic variables and transport coefficients into (2.1)–(2.4) and subtracting the base flow equations, we obtain nonlinear perturbation equations, correct up to cubic order, which can be put in the operator form:

$$\left(\frac{\partial}{\partial t}-\mathscr{L}\right)X=\mathscr{N}_2(X,X;\partial_t)+\mathscr{N}_3(X,X,X). \tag{3.2}$$

Here, $\mathscr{L}$ is the linear operator, $\mathscr{N}_2$ and $\mathscr{N}_3$ are the quadratic and cubic nonlinear terms, respectively, and $X=(\phi',u',v',T')^{\mathrm{T}}$ denotes the disturbance vector. The explicit forms of $\mathscr{N}_2$ and $\mathscr{N}_3$ are given in Appendix A (Appendix A is part of the supplementary material available at journals.cambridge.org/flm); note that in addition to standard quadratic terms involving disturbance variables and their spatial derivatives, $\mathscr{N}_2$ also contains terms involving time derivatives of X, which originate from inertial terms in momentum and energy equations as seen in (A3), (A5) and (A7). The linear stability operator is given by

$$\mathscr{L}=\begin{pmatrix} 0 & 0 & -\phi^0\dfrac{\partial}{\partial y} & 0 \\ \dfrac{\mu^0_\phi}{\phi^0H^2}\dfrac{\partial}{\partial y} & \dfrac{\mu^0}{\phi^0H^2}\dfrac{\partial^2}{\partial y^2} & -1 & \dfrac{\mu^0_T}{\phi^0H^2}\dfrac{\partial}{\partial y} \\ \dfrac{-p^0_\phi}{H^2\phi^0}\dfrac{\partial}{\partial y} & 0 & \dfrac{(2\mu^0+\lambda^0)}{H^2\phi^0}\dfrac{\partial^2}{\partial y^2} & \dfrac{-p^0_T}{H^2\phi^0}\dfrac{\partial}{\partial y} \\ \dfrac{2\left(\mu^0_\phi-\mathscr{D}^0_\phi\right)}{\phi^0\mathrm{dim}} & \dfrac{4\mu^0}{\phi^0\mathrm{dim}}\dfrac{\partial}{\partial y} & -\dfrac{2p^0}{\phi^0\mathrm{dim}}\dfrac{\partial}{\partial y} & \dfrac{2}{\phi^0\mathrm{dim}}\left(\dfrac{\kappa^0}{H^2}\dfrac{\partial^2}{\partial y^2}+\mu^0_T-\mathscr{D}^0_T\right) \end{pmatrix}. \tag{3.3}$$

The boundary conditions can be written in the matrix form as

$$\mathscr{B}X(y=\pm1/2)\equiv\begin{pmatrix} 0 & 0 & 0 & 0 \\ 0 & 1 & 0 & 0 \\ 0 & 0 & 1 & 0 \\ 0 & 0 & 0 & \dfrac{\partial}{\partial y} \end{pmatrix}\begin{pmatrix}\phi' \\ u' \\ v' \\ T'\end{pmatrix}=0, \tag{3.4}$$

with the boundary operator $\mathscr{B}$ as defined above.

3.1. *Linear adjoint system*

Neglecting nonlinearities, the linear stability equations can be presented as

$$\frac{\partial X}{\partial t}=\mathscr{L}X,\quad \text{with}\quad \mathscr{B}X=0. \tag{3.5}$$

The adjoint equation for this linear stability operator ($\mathscr{L}$) is

$$\frac{\partial X^\dagger}{\partial t} = \mathscr{L}^\dagger X^\dagger, \tag{3.6}$$

where $X^\dagger = [\phi^\dagger, u^\dagger, v^\dagger, T^\dagger]^{\mathrm{T}}$ is the adjoint eigenfunction and $\mathscr{L}^\dagger$ is the adjoint operator, which is calculated from the definition of the adjoint operator

$$\langle X^\dagger, \mathscr{L} X\rangle = \langle \mathscr{L}^\dagger X^\dagger, X\rangle. \tag{3.7}$$

In the above, the standard inner product has been defined as

$$\langle Y(y), Z(y)\rangle = \int_{-1/2}^{1/2} \tilde{Y}(y) Z(y)\,\mathrm{d}y = \int_{-1/2}^{1/2} \sum_{i=1}^{4} \tilde{y}_i(y) z_i(y)\,\mathrm{d}y, \tag{3.8}$$

for two complex-valued vector functions $Y(y) = [y_1, y_2, y_3, y_4]$ and $Z(y) = [z_1, z_2, z_3, z_4]$ on the interval $-1/2 \leqslant y \leqslant 1/2$, with the tilde denoting a complex conjugate quantity.

With the above definitions, the form of the adjoint operator can be shown to be related to the linear operator via

$$\mathscr{L}^\dagger \equiv \mathscr{L}^{\mathrm{T}}(\partial/\partial y \to -\partial/\partial y, \partial^2/\partial y^2; \phi^0, T^0, \ldots), \tag{3.9}$$

and the adjoint boundary conditions are

$$\mathscr{B} X^\dagger = 0, \tag{3.10}$$

with $\mathscr{B}$ being given by (3.4).

3.2. *Analytical solutions for fundamental mode and its adjoint*

Since the linear problem is invariant under arbitrary time translation $t \mapsto t + \text{constant}$, the normal mode solutions with complex frequency c are sought:

$$X(y, t) = \widehat{X}(y) \mathrm{e}^{ct}, \tag{3.11}$$

where $\widehat{X}(y) = [\hat{\phi}, \hat{u}, \hat{v}, \hat{T}](y)$ are unknown functions of y. This reduces the linearized system of partial differential equations to a set of ordinary differential equations:

$$c\boldsymbol{I}\,\widehat{X} = \boldsymbol{L}\widehat{X}, \quad \text{with} \quad \mathscr{B}\widehat{X} = 0, \tag{3.12}$$

where $\boldsymbol{L} \equiv \mathscr{L}(\mathrm{d}/\mathrm{d}y, \mathrm{d}^2/\mathrm{d}y^2, \ldots)$ is a linear ordinary differential operator, $\boldsymbol{I}$ is an identity operator and $c = c_r + \mathrm{i}\, c_i$ is a complex eigenvalue such that the flow is stable if $c_r > 0$, but unstable if $c_r < 0$, and neutrally stable if $c_r = 0$. It can be verified that this system of equations has analytical solutions (Alam & Nott 1998):

$$\left.\begin{aligned} (\hat{\phi}, \hat{T}) &= (\phi_1, T_1)\cos k_\beta (y \pm 1/2), \\ (\hat{u}, \hat{v}) &= (u_1, v_1)\sin k_\beta (y \pm 1/2), \end{aligned}\right\} \tag{3.13}$$

where $k_\beta = \beta\pi$, with $\beta = 1, 2, 3, \ldots$ being the mode numbers. Substituting the above solution in (3.12), we get an algebraic eigenvalue problem for linear stability:

$$c\boldsymbol{I}\, X_1 = \boldsymbol{Q}\, X_1, \tag{3.14}$$

where $X_1 = (\phi_1, u_1, v_1, T_1)$ represent the amplitude of the fundamental mode, and the elements of the matrix $\boldsymbol{Q}$ are straightforward to obtain from $\boldsymbol{L}$.

The classification of the mode number β as defined in (3.13) is given in terms of the number of zero-crossings of the density eigenfunction within $y \in (-1/2, 1/2)$ as shown in figure 2, which displays all four eigenfunctions of the first three modes

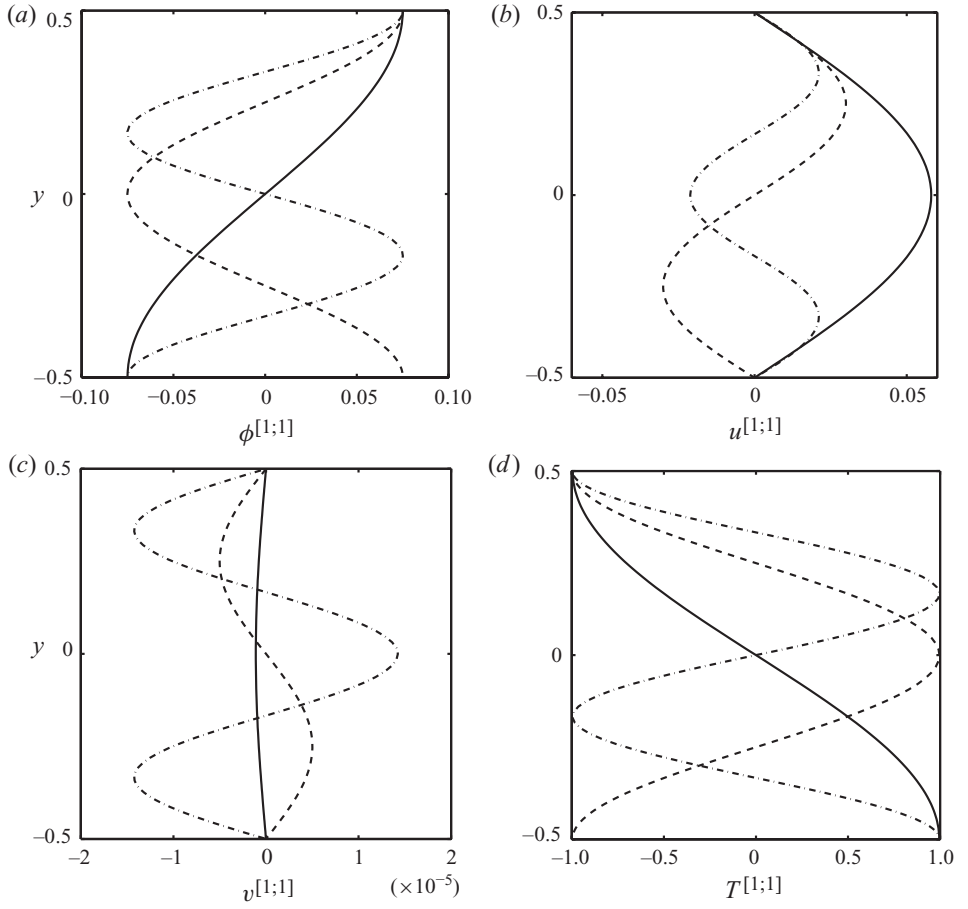

FIGURE 2. Linear eigenfunction profiles across the Couette gap for the first three modes $\beta = 1$ (solid line), 2 (dashed line) and 3 (dot-dashed line) for $\phi^0 = 0.15$, $H = 100$ and $e = 0.8$. (*a*) density, (*b*) streamwise velocity, (*c*) transverse velocity and (*d*) granular temperature.

$\beta = 1, 2, 3$ for $\phi = 0.15$, $H = 100$ and $e = 0.8$. It is clear that the eigenfunction for mode $\beta = 2$ can be obtained by joining the eigenfunction of mode $\beta = 1$ twice along the y-direction, and so on. Therefore, $k_\beta = \beta\pi$ in (3.13) can be considered as a 'discrete' wavenumber along the gradient (y) direction, with $k_1 = \pi$ being the wavenumber of the lowest-order mode: the higher the mode number (β) the larger is the 'gradient' wavenumber (k_β).

It can be verified that the adjoint system (3.6) satisfies the analytical solution of the linear stability problem, and hence we can write its solution in terms of sine and cosine functions as in (3.13):

$$\left.\begin{aligned} \phi^\dagger(y) &= \phi_1^\dagger \cos k_\beta(y \pm 1/2), \quad & u^\dagger(y) &= u_1^\dagger \sin k_\beta(y \pm 1/2), \\ v^\dagger(y) &= v_1^\dagger \sin k_\beta(y \pm 1/2), \quad & T^\dagger(y) &= T_1^\dagger \cos k_\beta(y \pm 1/2). \end{aligned}\right\} \tag{3.15}$$

Similar to linear eigenfunctions, we found that the adjoint eigenfunctions corresponding to the least stable shear-banding mode are real.

4. Nonlinear stability: amplitude expansion method and Landau coefficients

We follow the amplitude expansion method of Stuart (1960) and Watson (1960), which was later formalized by Reynolds & Potter (1967) in an elegant manner. This is an indirect method to arrive at the Landau–Stuart amplitude equation, and the related Landau coefficients are found by using the Fredholm integral or the solvability condition as detailed here. The nonlinear solutions are determined in terms of the basic wave and its distortion and harmonics of various orders.

As mentioned in the Introduction (§1), we have recently developed an order-parameter theory for the same problem using the centre-manifold reduction technique – the interested readers are directed to the supplementary information of our paper Shukla & Alam (2009) to understand the detailed methodology of that technique. While discussing the amplitude expansion method in §§4.1 and 4.2, we will remark on how and where the present method differs from the centre-manifold reduction technique.

In linear theory, we assume infinitesimal disturbances (basic wave) of the form

$$\mathbf{X}(y,t) = X^{[1;1]}(y)\mathrm{e}^{\mathrm{i}(\omega t)}\mathrm{e}^{at}, \tag{4.1}$$

where $a+\mathrm{i}\omega$ is the complex eigenvalue; e^{at} is the amplitude of the basic wave with a denoting its growth rate and ω is the frequency of the basic wave. (The superscript notation on the amplitude, $X^{[1;1]}$, of the linear eigenfunction is clarified in §4.2.2.) The flow is linearly unstable or stable or neutrally stable if a is positive or negative or zero, respectively.

In nonlinear stability, the amplitude of the disturbance, $A(t)$, is finite and time-dependent, which is taken to be the counterpart of the real exponential term in (4.1), i.e. $A(t)=\mathrm{e}^{at}$; moreover, the frequency of the basic wave, ω, is allowed to depend on the disturbance amplitude, i.e. $\omega\equiv\omega(A)$.

4.1. *Transformed nonlinear equations*

Let us use the following transformation (Reynolds & Potter 1967):

$$\theta=\omega t, \quad \omega=\omega(A), \quad A=A(t), \tag{4.2}$$

where $A(t)$ is the real amplitude of the disturbance such that $A(t)=\mathrm{e}^{at}$ for infinitesimal disturbances in the linear theory. The following fact is embodied in the above transformation: the growth rate and frequency will change with the finite size of the perturbation. Therefore, the partial time derivative can be transformed into

$$\frac{\partial}{\partial t}\rightarrow\frac{\mathrm{d}A}{\mathrm{d}t}\frac{\partial}{\partial A}+\left[\omega+\frac{\mathrm{d}\omega}{\mathrm{d}A}\left(t\frac{\mathrm{d}A}{\mathrm{d}t}\right)\right]\frac{\partial}{\partial\theta}. \tag{4.3}$$

This transformation is equivalent to a two time-scale transformation, where the first term in (4.3) represents a slow time scale (which implies that the perturbation amplitude $A(t)$ is a slowly varying function of time) and the second term represents a fast time scale.

The above transformation (4.3) is then inserted into streamwise-independent disturbance equations (3.2). For example, the x-momentum disturbance equation is transformed into

$$\phi^0\frac{\mathrm{d}A}{\mathrm{d}t}\frac{\partial u'}{\partial A}+\phi^0\left[\omega+\frac{\mathrm{d}\omega}{\mathrm{d}A}\left(t\frac{\mathrm{d}A}{\mathrm{d}t}\right)\right]\frac{\partial u'}{\partial\theta}+\phi^0 v' = \frac{1}{H^2}\left[\mu_\phi^0\frac{\partial\phi'}{\partial y}+\mu_T^0\frac{\partial T'}{\partial y}+\mu^0\frac{\partial^2 u'}{\partial y^2}\right]+\text{nonlinear terms}, \tag{4.4}$$

and the rest of the disturbance equations are transformed accordingly. All four equations can then be written in a compact form as

$$\left[\mathscr{M}(\partial_A, \partial_\theta; \omega) - \mathscr{L}(\partial_y, \partial_y^2; \phi^0, \ldots)\right] X = \mathscr{N}_2(X, X; \partial_t \to (\partial_A, \partial_\theta)) + \mathscr{N}_3(X, X, X). \quad (4.5)$$

Here $\mathscr{L}(\partial_y, \partial_y^2; \phi^0, \ldots)$ is the linear stability operator and $\mathscr{M}$ is a diagonal operator,

$$\mathscr{M} = \left[\frac{\mathrm{d}A}{\mathrm{d}t}\frac{\partial}{\partial A} + \left(\omega + \frac{\mathrm{d}\omega}{\mathrm{d}A}\left(t\frac{\mathrm{d}A}{\mathrm{d}t}\right)\right)\frac{\partial}{\partial\theta}\right]\boldsymbol{I}, \quad (4.6)$$

with $\boldsymbol{I}$ being the identity operator. In (4.5) the arguments of $\mathscr{N}_2(\cdot)$ contain partial derivatives ∂_A and ∂_θ that appear due to the replacement of the time derivative in the quadratic nonlinear terms in (A3), (A5) and (A7) via (4.3).

4.2. *Amplitude expansion method*

4.2.1. *Fourier expansion and transformed nonlinear equations*

To solve (4.5), now we look for solutions $X = X(y, A, \theta)$ in terms of the wall-normal distance (y), the amplitude of the perturbation (A) and the instantaneous position of the basic wave ($\theta = \omega t$). Let us consider the following Fourier expansion for the perturbation quantities (Watson 1960; Reynolds & Potter 1967):

$$X(y, A, \theta) = X^{(k)}(y, A)\,\mathrm{e}^{\mathrm{i}k\theta} + \tilde{X}^{(k)}(y, A)\,\mathrm{e}^{-\mathrm{i}k\theta}, \quad (4.7)$$

where the summation is taken over all positive integers $k \geqslant 0$, and the tilde over any quantity denotes its complex conjugate. This Fourier expansion (4.7) shows that, as mentioned before, the finite size of the perturbation will change both the frequency ($\sim\theta$ as embodied in the exponential term in (4.7)) and the growth rate ($\sim A$ as embodied in the amplitude function in (4.7)) of the perturbation.

Substituting (4.7) into the nonlinear perturbation equations (4.5) and collecting the coefficients of $\mathrm{e}^{\mathrm{i}k\theta}$, we obtain an infinite set of coupled nonlinear partial differential equations for each Fourier coefficient $X^{(k)}$, $k = 0, 1, 2, \ldots$. The matrix representation of these equations for $X^{(k)}(y, A) = (\phi^{(k)}, u^{(k)}, v^{(k)}, T^{(k)})^{\mathrm{T}}$ can be written as

$$\left(\mathscr{M}^{(k)} - \mathscr{L}\right) X^{(k)} = \mathscr{N}_2 + \mathscr{N}_3, \quad (4.8)$$

$$\mathscr{M}^{(k)} \equiv \mathscr{M}(\partial_A, \partial_\theta = \mathrm{i}k; \omega) = \left[\frac{\mathrm{d}A}{\mathrm{d}t}\frac{\partial}{\partial A} + \left(\omega + \frac{\mathrm{d}\omega}{\mathrm{d}A}\left(t\frac{\mathrm{d}A}{\mathrm{d}t}\right)\right)\mathrm{i}k\right]\boldsymbol{I}. \quad (4.9)$$

The boundary conditions are transformed into

$$\mathscr{B}X^{(k)} = 0 \quad \text{at} \quad y = \pm 1/2. \quad (4.10)$$

Because of the nonlinear interaction/coupling of different Fourier modes, the solution to the infinite set of partial differential equations (4.8) is difficult to ascertain. Focusing on small-amplitude (but finite) waves, a power-series solution in the amplitude A can be sought. This procedure amounts to choosing a variable separable solution in terms of a Taylor series in the perturbation amplitude which, in turn, helps to decouple the coupled system of nonlinear equations (4.8).

4.2.2. *Taylor expansion and superscript notation*

When the nonlinearities of governing equations are taken into account, the perturbation interacts with (i) itself, (ii) its complex conjugate and (iii) its higher-order harmonics, leading to the generation of harmonics and the corrections/distortions of various orders in the amplitude of perturbation. We require that the nonlinear problem for infinitesimal amplitudes ($A \to 0$) should reduce to the linear problem;

here $O(A)$ denotes the fundamental mode (linear eigenfunction), $O(1)$ denotes the mean flow, $O(A^2)$ consists of the second harmonic ($k=2$) as well as the distortion of the mean flow ($k=0$). The fundamental mode interacting with (i) itself and (ii) its complex conjugate leads to the generation of (i) the second harmonic and (ii) a distortion of the mean flow, respectively, both $O(A^2)$. Similarly, the interaction of (ia) the fundamental mode with the second harmonic and (ib) three fundamental modes generates the third harmonic ($k=3$), and (ii) the interaction of the fundamental mode with the distortion of the mean flow leads to the generation of the distortion of the fundamental mode ($k=1$), all three being $O(A^3)$. The above physical considerations suggest the following power-series expansion for the perturbation vector:

$$X^{(k)}(A, y) = A^n X^{[k;n]}(y), \quad \text{with} \quad k \geqslant 0,\ n \geqslant 1, \tag{4.11}$$

where $X^{[k;n]}(y) = (\phi^{[k;n]}, u^{[k;n]}, v^{[k;n]}, T^{[k;n]})^{\mathrm{T}}$ represent the spatially varying amplitude functions. We have followed Reynolds & Potter (1967) to identify the superscript notations and their bounds as indicated below:

$$(n) \Rightarrow n \geqslant 0, \quad [n] \Rightarrow n \geqslant 1, \quad \{n\} \Rightarrow n \geqslant 2, \quad n;m \Rightarrow n \leqslant m, \tag{4.12}$$

$$[k;n] \Rightarrow n \geqslant k, \quad k \geqslant 0, \quad n \geqslant 1, \tag{4.13}$$

$$\{k;n\} \Rightarrow n \geqslant k, \quad k \geqslant 1, \quad n \geqslant 2. \tag{4.14}$$

Note that the negative indices are not permitted and the lower bound on any index is greater than or equal to zero, depending on the type of the bracket/delimiter, ( ) or { } or [ ]. The last item in (4.12) asserts that a semicolon puts a limit on the first index which is bounded by its second index.

In the dual superscript notation for $X^{[k;n]}$ in (4.11), the first index (k) refers to a particular Fourier mode and the second index (n) indicates the order of a particular term as $O(A^n)$. To clarify this, let us consider the Taylor series expansion of the first three Fourier coefficients:

$$\left.\begin{aligned} X^{(1)}(y,t) &= A(t)\left(X^{[1;1]}(y) + A(t)^2 X^{[1;3]}(y) + \cdots\right), \\ X^{(0)}(y,t) &= A(t)^2\left(X^{[0;2]}(y) + A(t)^2 X^{[0;4]}(y) + \cdots\right), \\ X^{(2)}(y,t) &= A(t)^2\left(X^{[2;2]}(y) + A(t)^2 X^{[2;4]}(y) + \cdots\right). \end{aligned}\right\} \tag{4.15}$$

The leading term of the first ($k=1$) Fourier coefficient $X^{(k=1)}$ is $AX^{[1;1]}$, which is $O(A^{n=1})$, representing the fundamental mode; the next-order term in $X^{(k=1)}$ is $A^3X^{[1;3]}$, which represents the first correction/distortion of the fundamental mode and is $O(A^3)$, and $X^{[1;3]}$ is called the distortion of the fundamental mode. The zeroth ($k=0$) Fourier coefficient $X^{(k=0)}$ is related to the base/mean flow (which in our double index superscript notation would be $X^{[0;0]}(y) \equiv (\phi^0, u^0, v^0, T^0)^{\mathrm{T}}$, as in (2.10)). Therefore, the leading term in $X^{(0)}$ is $A^2X^{[0;2]}$, which represents the distortion of the mean flow, and the remaining terms are its subsequent higher-order corrections. Similarly, the leading term of the second Fourier coefficients $X^{(k=2)}$ is $A^2X^{[2;2]}$, which is the second harmonic, and the remaining terms are its subsequent higher-order corrections. It is clear from the above arguments and (4.15) that

$$X^{[k;n]} = 0, \quad \text{for odd} \quad (k+n) \tag{4.16}$$

in the power-series expansion (4.11)

The above superscript bracket notations (Reynolds & Potter 1967) are extremely useful in simplifying the algebra as well as in identifying a particular mode (i.e. a

fundamental or a harmonic of a particular order) and its modal interactions of any order.

4.2.3. *Landau equation and modal equations for* $X^{[k;n]}$

From the requirement that $A(t)$ be proportional to $e^{at}(a = a^{(0)})$ as $A \to 0$, it follows that

$$\frac{1}{A}\frac{\mathrm{d}A}{\mathrm{d}t} \to a^{(0)} \quad \text{as} \quad A \to 0. \tag{4.17}$$

This is the well-known limit of infinitesimal disturbances in linear stability theory. Since the amplitude for infinitesimal A must behave as in linear theory (i.e. grow/decay exponentially), we can write $(1/A)(\mathrm{d}A/\mathrm{d}t)$ as a power series in A:

$$A^{-1}\frac{\mathrm{d}A}{\mathrm{d}t} = a^{(0)} + Aa^{(1)} + A^2a^{(2)} + \cdots = A^n a^{(n)}, \tag{4.18}$$

where $a^{(0)}$ is an eigenvalue (growth rate) from the linear theory, and $a^{(n)}$ for odd n turns out to be zero (see below). For the nonlinear analysis, we are interested in $a^{(2)}$ or, in general, $a^{(n)}$ for even values of n. Similarly, we can write an expression for the terms involving frequency ω,

$$\omega + \frac{\mathrm{d}\omega}{\mathrm{d}A}\left(t\frac{\mathrm{d}A}{\mathrm{d}t}\right) = b^{(0)} + Ab^{(1)} + A^2b^{(2)} + \cdots = A^n b^{(n)}, \tag{4.19}$$

where $b^{(0)}$ is an eigenvalue (frequency) from the linearized theory, $b^{(n)}$ for odd n turns out to be zero and $b^{(n)}$ for even values of n are needed for the nonlinear analysis. Note that $b^{(2)}$ would represent the leading-order nonlinear correction to the frequency of oscillation.

It is clear that the Landau equation is postulated to hold in the present formalism of the amplitude expansion method (Stuart 1960; Watson 1960; Reynolds & Potter 1967). This is in contrast to the centre-manifold reduction (Carr 1981) wherein the Landau equation is derived from the evolution equation of the slow mode by taking its inner product with the adjoint linear eigenfunction (Shukla & Alam 2009). This is one of the main differences between the 'direct' method of centre-manifold reduction and the 'indirect' method of the amplitude expansion technique (see the last paragraph of § 4.5 for other major differences).

Inserting (4.11)–(4.19) into (4.8) and equating the coefficients of A^n, we get an infinite set of inhomogeneous equations for $X^{[k;n]} = [\phi^{[k;n]}, u^{[k;n]}, v^{[k;n]}, T^{[k;n]}]^{\mathrm{T}}$:

$$\left.\begin{aligned} \boldsymbol{L}_{kn}X^{[k;n]} &= -c^{[n-1]}X^{[1;1]}\delta_{k1} + G_{kn}, \\ c^{[n-1]} &= a^{[n-1]} + \mathrm{i}b^{[n-1]}, \\ G_{kn} &= -\left(ma^{[n-m]} + \mathrm{i}kb^{[n-m]}\right)X^{\{k;m\}} + E_{kn}/(1+\delta_{k0}) + F_{kn}, \\ \boldsymbol{L}_{kn} &= \left(na^{(0)} + \mathrm{i}kb^{(0)}\right)\boldsymbol{I} - \boldsymbol{L}, \end{aligned}\right\} \tag{4.20}$$

where $\boldsymbol{L} \equiv \mathscr{L}(\mathrm{d}/\mathrm{d}y, \mathrm{d}^2/\mathrm{d}y^2, \ldots)$ is the linear stability operator as in (3.3), $c^{[n-1]}$ values are Landau coefficients, the vector G_{kn} represents a sum of linear and nonlinear (quadratic and cubic) terms, $\boldsymbol{I}$ is the identity operator and δ_{kj} is the Kronecker delta; for superscript notations used in the above equation, see (4.11)–(4.13). In (4.20), the factor $1/(1+\delta_{k0})$ with E_{kn} arises from the product of two Fourier series in which the zeroth-order terms are multiplied by a factor 2; F_{kn} represents cubic nonlinear terms that arise from the product of three Fourier series. Note that the nonlinear terms E_{kn}

and F_{kn} are vector-valued functions:

$$E_{kn} = \left[E^1_{kn}, E^2_{kn}, E^3_{kn}, E^4_{kn}\right]^{\mathrm{T}} \quad \text{and} \quad F_{kn} = \left[F^1_{kn}, F^2_{kn}, F^3_{kn}, F^4_{kn}\right]^{\mathrm{T}}, \tag{4.21}$$

where the superscripts 1, 2, 3 and 4 refer to terms that originate from the continuity, x-momentum, y-momentum and granular energy equations, respectively. Furthermore, we can decompose the quadratic nonlinear terms E_{kn} as

$$E_{kn} = E^{\theta}_{kn} + E^{y}_{kn} \equiv E^{t}_{kn} + E^{y}_{kn}, \tag{4.22}$$

where $E^{\theta}_{kn} = E^{t}_{kn}$ corresponds to θ-dependent terms that involve the derivatives of t, and E^{y}_{kn} corresponds to terms that are y-dependent and their derivatives with respect to y. Note that the term E^{t}_{kn}, corresponding to the time-dependent part of disturbance equations, is the product of a Fourier series and a time derivative of a Fourier series that involves Landau equation (4.18). The above system of equations (4.20) is to be solved with the following boundary conditions:

$$\mathscr{B}X^{[k;n]} = 0 \quad \text{at} \quad y = \pm 1/2. \tag{4.23}$$

Equations (4.20) with boundary conditions (4.23) embody all necessary information for the nonlinear analysis of the granular plane Couette flow as discussed in §§ 4.3–4.5. We have reduced our nonlinear stability problem to a sequence of linear inhomogeneous differential equations (4.20) for $X^{[k;n]}$ and each of which can be solved sequentially if we know the Landau coefficients $c^{[n-1]}$ along the way. The latter can be obtained using the Fredholm alternative or the solvability condition of inhomogeneous differential equations discussed in § 4.5.

4.3. *Linear disturbance: fundamental mode*

At $O(A)$ we get back the linear problem for the fundamental mode $X^{[1;1]}$ by substituting $k = n = 1$ into (4.20):

$$\boldsymbol{L}_{11}X^{[1;1]} = 0 \quad \Rightarrow \quad \boldsymbol{L}X^{[1;1]} = c^{(0)}\boldsymbol{I}X^{[1;1]}, \tag{4.24}$$

where $\boldsymbol{L}$ is the linear stability operator. This equation is the same as (3.12) with $c = c^{(0)}$ and $\widehat{X} = X^{[1;1]}$.

4.4. *Mean-flow distortion and the second harmonic*

At $O(A^2)$, we get equations for the mean-flow distortion and the second harmonic. Substituting $k = n = 2$ into (4.20), we get

$$\boldsymbol{L}_{22}X^{[2;2]} \equiv \left[2(a^{(0)} + \mathrm{i}b^{(0)})\boldsymbol{I} - \boldsymbol{L}\right]X^{[2;2]} = G_{22} \equiv E_{22} \tag{4.25}$$

with the boundary conditions $\mathscr{B}X^{[2;2]} = 0$ at $y = \pm 1/2$. Here, $G_{22} = N_2(X^{[1;1]}, X^{[1;1]}) = E_{22}$ is the product of two fundamental modes. Note that there is no cubic nonlinear contribution at second order (i.e. $F_{22} = 0$).

Substituting $k = 0$ and $n = 2$ into (4.20), we get, at $O(A^2)$,

$$\boldsymbol{L}_{02}X^{[0;2]} \equiv \left[2a^{(0)}\boldsymbol{I} - \boldsymbol{L}\right]X^{[0;2]} = G_{02} \equiv E_{02}/2, \tag{4.26}$$

where $G_{02} = G_{02}(\tilde{X}^{[1;1]}, X^{[1;1]})$, with boundary conditions $\mathscr{B}X^{[0;2]} = 0$ at $y = \pm 1/2$. The explicit functional form of G_{02} is

$$G_{02} = 0.5\left[N_2(\tilde{X}^{[1;1]}, X^{[1;1]}) + N_2(X^{[1;1]}, \tilde{X}^{[1;1]})\right]. \tag{4.27}$$

Note that $X^{[0;2]}$ is always real. To verify this, let us write the complex conjugate equation for $X^{[0;2]}$,

$$\boldsymbol{L}_{02}\tilde{X}^{[0;2]} = \tilde{G}_{02}, \tag{4.28}$$

where $\boldsymbol{L}_{02} = \tilde{\boldsymbol{L}}_{02}$, and $\tilde{G}_{02}$ is given by

$$\tilde{G}_{02} = 0.5\big[N_2(X^{[1;1]}, \tilde{X}^{[1;1]}) + N_2(\tilde{X}^{[1;1]}, X^{[1;1]})\big] \equiv G_{02}. \tag{4.29}$$

This immediately implies that $X^{[0;2]}$ is real:

$$X^{[0;2]} = \tilde{X}^{[0;2]}. \tag{4.30}$$

In § 7.1, we will further prove that $X^{[0;2]} = X^{[2;2]}$, i.e. the base flow distortion and the second harmonic are equal for the shear-banding mode.

4.5. *Distortion of the fundamental mode and the first Landau coefficient*

At $O(A^3)$, we get an equation for the distortion of the fundamental mode $X^{[1;3]}$ by substituting $k = 1$ and $n = 3$ into (4.20):

$$\boldsymbol{L}_{13}X^{[1;3]} \equiv \big[(3a^{(0)} + \mathrm{i}b^{(0)})\boldsymbol{I} - \boldsymbol{L}\big]X^{[1;3]} = -c^{(2)}X^{[1;1]} + G_{13}. \tag{4.31}$$

The expression for the inhomogeneous term G_{13} is

$$\begin{aligned} G_{13} &= N_2(X^{[0,2]}, X^{[1;1]}) + N_2(\tilde{X}^{[0,2]}, X^{[1;1]}) + N_2(X^{[1;1]}, X^{[0,2]}) + N_2(X^{[1;1]}, \tilde{X}^{[0,2]}) \\ &\quad + N_2(\tilde{X}^{[1,1]}, X^{[2;2]}) + N_2(X^{[2;2]}, \tilde{X}^{[1,1]}) + N_3(\tilde{X}^{[1,1]}, X^{[1;1]}, X^{[1;1]}) \\ &\quad + N_3(X^{[1;1]}, \tilde{X}^{[1,1]}, X^{[1;1]}) + N_3(X^{[1;1]}, X^{[1;1]}, \tilde{X}^{[1,1]}) \\ &= 2\big[N_2(X^{[0,2]}, X^{[1;1]}) + N_2(X^{[1;1]}, X^{[0,2]})\big] + N_2(\tilde{X}^{[1,1]}, X^{[2;2]}) + N_2(X^{[2;2]}, \tilde{X}^{[1,1]}) \\ &\quad + N_3(\tilde{X}^{[1,1]}, X^{[1;1]}, X^{[1;1]}) + N_3(X^{[1;1]}, \tilde{X}^{[1,1]}, X^{[1;1]}) + N_3(X^{[1;1]}, X^{[1;1]}, \tilde{X}^{[1,1]}) \end{aligned} \tag{4.32}$$

and the boundary conditions are $\mathscr{B}X^{[1;3]} = 0$ at $y = \pm 1/2$. In the above equation, the quadratic and cubic nonlinear terms represent E_{kn} and F_{kn}, respectively, in (4.20).

In (4.31), the first Landau coefficient $c^{(2)}$ is unknown, which can be found by invoking the solvability condition

$$c^{(2)} = a^{(2)} + \mathrm{i}b^{(2)} = \frac{\displaystyle\int_{-1/2}^{1/2} \tilde{X}^{\dagger} G_{13}\,\mathrm{d}y}{\displaystyle\int_{-1/2}^{1/2} \tilde{X}^{\dagger} X^{[1;1]}\,\mathrm{d}y}, \tag{4.33}$$

where $X^{\dagger}$ is the adjoint linear eigenfunction that corresponds to the solution of (3.6). The solvability condition or the Fredholm alternative asserts that the inhomogeneous part of differential equations (4.31) must be orthogonal to the adjoint of the associated homogeneous problem – this guarantees the uniqueness of the solution to the inhomogeneous differential equations (4.31).

Similar to (4.33), we can write down a general expression for Landau coefficients of any order, $c^{(n)}$, in terms of an integral involving inhomogeneous terms, G_{kn}, of (4.20). It is straightforward to verify from (4.16) that $G_{kn} = 0$ when $(k + n)$ is odd, and hence $c^{(n)}$ vanishes for all odd $n = 1, 3, 5, \ldots$. The next non-zero coefficient is $c^{(4)}$, which is called the second Landau coefficient. In this paper, we restrict ourselves to calculating only the first Landau coefficient $c^{(2)}$ from (4.33).

Note that the expression for the first Landau coefficient obtained from the centre-manifold reduction ((9) in Shukla & Alam 2009) is exactly the same as (4.33) with the normalization $\langle \tilde{X}^{\dagger}, X^{[1;1]} \rangle = 1$. Before proceeding further, note an important difference between the amplitude expansion method and the centre-manifold reduction with respect to the calculation of this first Landau coefficient. It is clear from

the above discussion that in the amplitude expansion method, the first Landau coefficient (4.33) is determined from the solvability condition of the inhomogeneous differential equation for the distortion of the fundamental mode ($X^{[1;3]}$) that appears at cubic order as in (4.31). This may be contrasted with the calculation of the same from the centre-manifold reduction (see Shukla & Alam 2009), where our starting point is an evolution equation for the slow/critical mode which is obtained from a spectral decomposition of the linear operator in terms of slow and fast modes, with the fundamental mode being called the 'slow' mode (because the growth rate of the fundamental mode is close to zero, this is the slowest decaying mode) and the remaining eigenvalues (having large negative growth rates and hence fast decaying) as 'fast' modes. The inner product of the evolution equation for the slow mode with the adjoint of the linear eigenfunction then leads to the well-known Landau equation, and the coefficient of the cubic term (A^3) in the Landau equation is simply the first Landau coefficient, which is expressed in terms of an inner product of certain nonlinear terms and the adjoint linear eigenfunction. The evolution equations for fast/slave modes are used to concurrently determine the base-flow distortion and the second harmonic that are needed to evaluate the nonlinear terms in the expression for the first Landau coefficient. The related mathematical details can be found in the supplementary information of Shukla & Alam (2009) and hence we do not repeat them here for the sake of brevity.

5. Symmetries of linear and nonlinear modes

Before embarking on the analytical/numerical solution procedure of (4.23), (4.24), (4.25), (4.30) and (4.33), here we analyse certain symmetries of the linear ($X^{[1;1]}$) and nonlinear modes ($X^{[2;2]}$, $X^{[0;2]}$ and $X^{[1;3]}$) up to the cubic order.

First, let us consider the base state solution of uniform shear with constant density and granular temperature. The base state equations remain invariant under the following transformation:

$$\phi^0(-y) = \phi^0(y), \quad u^0(-y) = -u^0(y), \quad T^0(-y) = T^0(y). \tag{5.1}$$

This symmetry about the midplane $y = 0$ of the base state solution (2.10) implies that the velocity is antisymmetric about $y = 0$ and the density and granular temperature are symmetric about $y = 0$.

The linear disturbance equations for the fundamental mode and the related boundary conditions satisfy the following two symmetry groups (Alam & Nott 1998):

$$\left.\begin{aligned} \phi^{[1;1]}(y) &= \phi^{[1;1]}(-y), \qquad u^{[1;1]}(y) = -u^{[1;1]}(-y), \\ v^{[1;1]}(y) &= -v^{[1;1]}(-y), \qquad T^{[1;1]}(y) = T^{[1;1]}(-y), \end{aligned}\right\} \tag{5.2}$$

and

$$\left.\begin{aligned} \phi^{[1;1]}(y) &= -\phi^{[1;1]}(-y), \qquad u^{[1;1]}(y) = u^{[1;1]}(-y), \\ v^{[1;1]}(y) &= v^{[1;1]}(-y), \qquad T^{[1;1]}(y) = -T^{[1;1]}(-y), \end{aligned}\right\} \tag{5.3}$$

where the former preserves the symmetry of the base state solution (5.1), and the latter breaks (5.1).

It follows from the symmetries of the fundamental mode that the interaction of two fundamentals would give rise to the following symmetry for the second harmonic:

$$\left.\begin{aligned} \phi^{[2;2]}(y) &= \phi^{[2;2]}(-y), \qquad u^{[2;2]}(y) = -u^{[2;2]}(-y), \\ v^{[2;2]}(y) &= -v^{[2;2]}(-y), \qquad T^{[2;2]}(y) = T^{[2;2]}(-y). \end{aligned}\right\} \tag{5.4}$$

This, of course, preserves the symmetry (5.1) of the base state solution. The distortion of the mean flow, $X^{[0,2]}$, also follows the same symmetry of the base state since $X^{[0,2]}$ appears at the quadratic order $O(A^2)$.

Similarly, the distortion of the fundamental mode, $X^{[1,3]}$, satisfies the following symmetries:

$$\left.\begin{aligned} \phi^{[1;3]}(y) &= \phi^{[1;3]}(-y), \qquad u^{[1;3]}(y) = -u^{[1;3]}(-y), \\ v^{[1;3]}(y) &= -v^{[1;3]}(-y), \qquad T^{[1;3]}(y) = T^{[1;3]}(-y), \end{aligned}\right\} \tag{5.5}$$

and

$$\left.\begin{aligned} \phi^{[1;3]}(y) &= -\phi^{[1;3]}(-y), \qquad u^{[1;3]}(y) = u^{[1;3]}(-y), \\ v^{[1;3]}(y) &= v^{[1;3]}(-y), \qquad T^{[1;3]}(y) = -T^{[1;3]}(-y). \end{aligned}\right\} \tag{5.6}$$

The above symmetry groups can be understood from the fact that the fundamental mode is $O(A)$ and the interaction of two fundamentals gives rise to the terms $O(A^2)$, and so forth. Thus, the second harmonic $X^{[2;2]}$ admits a symmetry which is the product of symmetries of the fundamental mode. Similarly, the symmetry of the distortion of the fundamental ($O(A^3)$) would follow the product of symmetries of the fundamental and the second harmonic.

6. Numerical method: spectral collocation and Gauss–Chebyshev quadrature

In § 4, we have reduced the nonlinear stability problem to a sequence of systems of inhomogeneous linear differential equations for the fundamental mode and its distortions and higher-order harmonics. The general form of this system of equations is

$$\boldsymbol{L}_{kn} X^{[k;n]} = -c^{[n-1]} X^{[k;n]} \delta_{k1} + G_{kn}, \quad \text{with} \quad k \geqslant 0,\ n \geqslant 1, \tag{6.1}$$

where $\boldsymbol{L}_{kn}$ is the linear operator, $c^{[n-1]}$ are the Landau coefficients and G_{kn} denotes the nonlinear terms. We have developed a spectral-based numerical method to solve the above problem and a brief description of this numerical method is given below.

For the linear stability problem (4.24), we need to solve the linearized perturbation equations along with homogeneous boundary conditions. All four equations have been discretized along the y-direction by implementing the staggered-grid spectral collocation method that uses Chebyshev polynomials as a basis set. More specifically, the mass balance equation is collocated at Gauss points and the momentum and energy equations at Gauss–Lobatto points. The interpolation matrices of spectral accuracy are then used to interpolate between the variables at Gauss (density) and Gauss–Lobatto (velocity and granular temperature) points. For details on the spectral collocation technique, the reader is referred to Canuto *et al.* (1988) and Fornberg (1998). The discretized form of perturbation equations, along with boundary conditions, is formulated as a generalized matrix eigenvalue problem of the form

$$\boldsymbol{A} X^{[1;1]} = c^{(0)} \boldsymbol{B} X^{[1;1]}, \tag{6.2}$$

where $c^{(0)}$ is the linear eigenvalue and $X^{[1;1]}$ is the discrete representation of linear eigenfunction; $\boldsymbol{A}$ and $\boldsymbol{B}$ are square matrices of order $(4M + 3)$, where M denotes the number of collocation points (i.e. the degree of the Chebyshev polynomial). The eigenvalues of the generalized eigenvalue problem are determined by the QZ-algorithm of MATLAB software. The eigenvectors $X^{[1;1]}$ are normalized by dividing it by a component of the vector $X^{[1;1]}$ having the maximum absolute value. Another part of the linear stability problem is to solve the associated adjoint system. Using

the same spectral method, the adjoint system has been discretized and solved for the adjoint eigenfunction $X^\dagger$ and its adjoint eigenvalue $c^{(0)^\dagger} = c^{\tilde{(0)}}$. Recall that the adjoint eigenfunction is used in the solvability condition (4.33) to calculate the first Landau coefficient.

For nonlinear stability, we need to solve the related inhomogeneous differential equations, (4.25), (4.26) and (4.31), and the solvability condition (4.33). We can subdivide these nonlinear calculations into two parts: one is to solve $\mathscr{A}X = b$ type equations ((4.25), (4.26) and (4.31)), and the other is to calculate the first Landau coefficient using the solvability condition (4.33). Similar to the linear eigenvalue problem, the higher-order inhomogeneous system of differential equations is discretized using the same staggered-grid spectral collocation method, where the continuity equation is evaluated at Gauss points and other equations are at Gauss–Lobatto points. The resulting square matrix $\mathscr{A}$ in $\mathscr{A}X = b$ turns out to be dense, unstructured, unsymmetric and ill-conditioned; thus, the method of the Gaussian elimination is not a good choice to solve these algebraic equations. We employed the method of singular value decomposition (Press *et al.* 1992) for solving $\mathscr{A}X = b$ system in each case of (4.25), (4.26) and (4.31).

The second part of nonlinear computations is related to evaluating the solvability condition (4.33) to determine the first Landau coefficient: this is a ratio of two definite integrals. These integrations are calculated using the Gauss–Chebyshev quadrature: the Gaussian quadrature using the Chebyshev polynomial as an interpolating polynomial is called the Gauss–Chebyshev quadrature. Next, we briefly discuss an accurate quadrature formula at Gauss–Lobatto points (Hanifi, Schmid & Henningson 1996) to evaluate the above-mentioned integrals. In the spectral collocation method, we approximate the unknown variables in terms of the Chebyshev polynomials of degree M,

$$f(\zeta) = \sum_{\alpha=0}^{M} a_\alpha T_\alpha(\zeta), \tag{6.3}$$

where $T_\alpha(\zeta) = \cos(\alpha \cos^{-1}(\zeta))$. The Chebyshev polynomials are then evaluated at the extrema of the Mth-order Chebyshev polynomial, called Gauss–Lobatto points, given by

$$\zeta_j = \cos\left(\frac{j\pi}{M}\right), \tag{6.4}$$

where $j = 0, \ldots, M$.

The general rule for Gaussian quadratures is

$$\int_{-1}^{1} f(\zeta)\,\mathrm{d}\zeta = \sum_{j=0}^{M} w(\zeta_j) f(\zeta_j), \tag{6.5}$$

where $w(\zeta_j)$ is the weight function and ζ_j are called nodes. To derive the Gauss–Chebyshev quadrature formula, we need to find weight functions on the Chebyshev grid (i.e. on the Gauss–Lobatto grid). Now we make use of the discrete orthogonality condition of the Chebyshev polynomials, which reads as

$$\langle f, g \rangle = \sum_{j=0}^{M} b_j f(\zeta_j) g(\zeta_j), \tag{6.6}$$

where $b_0 = b_M = 1/2, b_j = 1$ for $0 < j < M$, and ζ_j are the Gauss–Lobatto points as defined in (6.4). From this definition, it follows that

$$\langle T_\alpha(\zeta), T_\gamma(\zeta)\rangle = \begin{cases} 0 & \alpha \neq \gamma, \\ M & \alpha = \gamma = 0, M, \\ M/2 & \alpha = \gamma \neq 0, M, \end{cases} \tag{6.7}$$

which can be used to obtain the expansion coefficients a_α in (6.3):

$$a_\alpha = \frac{c_\alpha}{M} \sum_{j=0}^{M} b_j f(\zeta_j) T_\alpha(\zeta_j), \tag{6.8}$$

where $c_0 = c_M = 1$ and $c_\alpha = 2$ for all $0 < \alpha < M$. Therefore, the expansion formula (6.3) simplifies to

$$f(\zeta) = \sum_{\alpha=0}^{M} a_\alpha T_\alpha(\zeta) = \sum_{\alpha=0}^{M} c_\alpha T_\alpha(\zeta) \sum_{j=0}^{M} \frac{b_j}{M} f(\zeta_j) T_\alpha(\zeta_j), \tag{6.9}$$

which, upon integration with respect to ζ, leads to

$$\int_{-1}^{1} f(\zeta)\,\mathrm{d}\zeta = \frac{1}{M} \sum_{j=0}^{M} b_j f(\zeta_j) \sum_{\alpha=0}^{M} c_\alpha T_\alpha(\zeta_j) \int_{-1}^{1} T_\alpha(\zeta)\,\mathrm{d}\zeta, \tag{6.10}$$

where

$$\int_{-1}^{1} T_\alpha(\zeta)\,\mathrm{d}\zeta = \begin{cases} 0 & \alpha \text{ odd}, \\ \dfrac{2}{1-\alpha^2} & \alpha \text{ even}. \end{cases} \tag{6.11}$$

This immediately yields an expression for the weight function as defined via (6.5):

$$w(\zeta_j) = \frac{b_j}{M} \left\{ 2 + \sum_{\alpha=2}^{M} c_\alpha \frac{1 + (-1)^\alpha}{1-\alpha^2} \cos\left(\frac{\alpha j \pi}{M}\right) \right\}. \tag{6.12}$$

If a mapping $\zeta = \zeta(y)$ is used to transform the physical domain $y \in [y_1, y_2]$ into the Chebyshev domain $\zeta \in [-1, 1]$, then the expression for the weight function becomes

$$w(\zeta_j) = \frac{b_j}{M} \sum_{\alpha=0}^{M} c_\alpha \cos\left(\frac{\alpha j \pi}{M}\right) \int_{-1}^{1} T_\alpha(\zeta) \frac{\mathrm{d}y}{\mathrm{d}\zeta}\,\mathrm{d}\zeta. \tag{6.13}$$

In the present problem the physical domain is $y = [-1/2, 1/2]$ and hence we can assume a mapping $\zeta = 2y$, and the Gauss–Chebyshev quadrature formula can be rewritten as

$$\int_{-1/2}^{1/2} f(y)\,\mathrm{d}y = \sum_{j=0}^{M} w(\zeta_j) f(\zeta_j), \tag{6.14}$$

where $w(\zeta_j)$ is given by (6.13) with $\mathrm{d}y/\mathrm{d}\zeta = 1/2$.

To numerically evaluate the solvability condition (4.33), we first calculate each integrand at the Gauss–Lobatto points (where the terms related to the continuity equation are interpolated from Gauss points to Gauss–Lobatto points) and then take the weighted summation as in (6.14). For the present problem, the above quadrature formula has been compared with two other composite integration methods, namely

Symbols	Definition
ϕ^0	Mean density or solid fraction (the volume fraction of particles)
$H = \overline{h}/\overline{d}$	Ratio between the Couette gap and the particle diameter
e	Restitution coefficient
$k_\beta = \beta\pi$	'Discrete' wavenumber along the y-direction, (3.13)
$\beta = 1, 2, 3, \ldots$	Mode number, (3.13), (7.1)
$a^{(0)}$	Growth rate of the fundamental mode, (4.1), (4.16), (4.17), (8.9)
$a^{(2)}$	Real part of the first Landau coefficient, (4.17), (4.32), (8.9)
M	Number of collocation points, (6.4), (6.13)
H_c	Critical Couette gap, (8.4)
ϕ_c	Critical mean density, (8.5)
$A = A_e$	Equilibrium amplitude, (8.9)
H^*	$H\beta^{-1}(1-e^2)^{1/2}$, (8.19)

TABLE 1. Control parameters for stability.

Simpson and trapezoidal quadrature rules. It has been verified that the Gauss–Chebyshev quadrature converges with about $M = 75$ collocation points, while to get the same accuracy using the Simpson quadrature we need to use $M > 200$ grid points. This superior convergence of the Gauss–Chebyshev quadrature is presumably due to the spectral accuracy of the underlying scheme (Canuto *et al.* 1988; Hanifi *et al.* 1996). Table 1 summarizes all dimensionless parameters that we will frequently refer to while presenting our results in §§ 7–9.

7. Analytical solution and comparison with numerical (spectral) solution

The underlying symmetries of the fundamental mode and its nonlinear corrections as discussed in § 5, together with the analytical solution of the fundamental mode (Alam & Nott 1998), helped us to solve the nonlinear problem analytically as discussed in §§ 7.1–7.3. As mentioned above, this problem was tackled numerically in our recent papers Shukla & Alam (2008, 2009), even though the order-parameter equation was derived there using another method, namely, the centre-manifold reduction technique. Apart from providing new analytical solutions in the present paper, the spectral-based numerical technique, as detailed in § 6, is also validated here against our analytical solutions for harmonics and the first Landau coefficient.

7.1. *Solution for second harmonic and mean-flow distortion*

It can be verified that there exists an analytical solution for the second harmonic:

$$\left.\begin{aligned} \phi^{[2;2]}(y) &= \phi_2 \cos k_{2\beta}(y \pm 1/2), \\ u^{[2;2]}(y) &= u_2 \sin k_{2\beta}(y \pm 1/2), \\ v^{[2;2]}(y) &= v_2 \sin k_{2\beta}(y \pm 1/2), \\ T^{[2;2]}(y) &= T_2 \cos k_{2\beta}(y \pm 1/2) + T^{mean}_{k_{2\beta}}, \end{aligned}\right\} \tag{7.1}$$

where $k_{2\beta} = 2\beta\pi$, with $\beta = 1, 2, 3, \ldots$ and $X_{22} = [\phi_2, u_2, v_2, T_2]$ is the amplitude of the second harmonic. The mean term in the disturbance energy equation is calculated from

$$T^{mean}_{k_{2\beta}} = \frac{f_{nl}}{f_l}, \tag{7.2}$$

where f_{nl} denotes nonlinear terms and f_l are related to linear terms:

$$f_{nl} = -\frac{1}{2\phi^0}\left(-v_1 T_1 k_\beta + c^{(0)}\phi_1 T_1\right) + \frac{1}{\phi^0 \mathrm{dim}}\left[-k_\beta\left(p^0_\phi \phi_1 + p^0_T T_1\right)v_1 + 2\mu^0 k_\beta^2\left(v_1^2 + \frac{1}{2}u_1^2\right) + \left(\frac{1}{2}\mu^0_{\phi\phi}\phi_1^2 + \frac{1}{2}\mu^0_{TT}T_1^2 + \mu^0_{\phi T}\phi_1 T_1\right) + 2k_\beta u_1\left(\mu^0_\phi\phi_1 + \mu^0_T T_1\right) + \lambda^0 k_\beta^2 v_1^2 - \left(\frac{1}{2}\mathscr{D}^0_{\phi\phi}\phi_1^2 + \frac{1}{2}\mathscr{D}^0_{TT}T_1^2 + \mathscr{D}^0_{\phi T}\phi_1 T_1\right)\right], \quad (7.3)$$

$$f_l = 2c^{(0)} - \frac{2}{\phi^0 \mathrm{dim}}\left(\mu^0_T - \mathscr{D}^0_T\right). \quad (7.4)$$

The modal amplitude of the second harmonic, $X_{22} = [\phi_2, u_2, v_2, T_2]$, satisfies the following algebraic matrix equation:

$$L^\beta_{22} X_{22} = G^\beta_{22}, \quad (7.5)$$

where $L^\beta_{22} = 2(a^{(0)} + \mathrm{i}b^{(0)})I - L^\beta$ with

$$L^\beta = \begin{pmatrix} 0 & 0 & -\phi^0 k_{2\beta} & 0 \\ -\dfrac{k_{2\beta}\mu^0_\phi}{\phi^0 H^2} & -\dfrac{k^2_{2\beta}\mu^0}{\phi^0 H^2} & -1 & -\dfrac{k_{2\beta}\mu^0_T}{\phi^0 H^2} \\ \dfrac{k_{2\beta}p^0_\phi}{H^2\phi^0} & 0 & -\dfrac{k^2_{2\beta}(2\mu^0+\lambda^0)}{H^2\phi^0} & \dfrac{k_{2\beta}p^0_T}{H^2\phi^0} \\ \dfrac{2(\mu^0_\phi - \mathscr{D}^0_\phi)}{\phi^0 \mathrm{dim}} & \dfrac{4k_{2\beta}\mu^0}{\phi^0\mathrm{dim}} & -\dfrac{2k_{2\beta}p^0}{\phi^0\mathrm{dim}} & \dfrac{2}{\phi^0\mathrm{dim}}\left(-k^2_{2\beta}\dfrac{\kappa^0}{H^2} + \mu^0_T - \mathscr{D}^0_T\right) \end{pmatrix}, \quad (7.6)$$

and the nonlinear inhomogeneous terms, $G^\beta_{22} = [G^{1\beta}_{22}, G^{2\beta}_{22}, G^{3\beta}_{22}, G^{4\beta}_{22}]$, are

$$G^{1\beta}_{22} = -k_\beta \phi_1 v_1, \quad (7.7)$$

$$G^{2\beta}_{22} = \frac{1}{2}\left[-\frac{1}{\phi^0}\left(\phi^0 v_1 u_1 k_\beta + \phi_1 v_1 + c^{(0)}\phi_1 u_1\right) + \frac{1}{\phi^0 H^2}\left(-k_\beta^2\left(\mu^0_\phi\phi_1 + \mu^0_T T_1\right)u_1 - k_\beta\left(\mu^0_{\phi\phi}\phi_1^2 + \mu^0_{TT}T_1^2 + 2\mu^0_{\phi T}\phi_1 T_1\right) - k_\beta^2\left(\mu^0_\phi\phi_1 + \mu^0_T T_1\right)u_1\right)\right], \quad (7.8)$$

$$G^{3\beta}_{22} = \frac{1}{2}\left[-\frac{1}{\phi^0}\left(k_\beta\phi^0 v_1^2 + c^{(0)}\phi_1 v_1\right) + \frac{1}{\phi^0 H^2}\left(k_\beta\left(p^0_{\phi\phi}\phi_1^2 + p^0_{TT}T_1^2 + 2p^0_{\phi T}\phi_1 T_1\right) - 4k_\beta^2\left(\mu^0_\phi\phi_1 + \mu^0_T T_1\right)v_1 - 2k_\beta^2\left(\lambda^0_\phi\phi_1 + \lambda^0_T T_1\right)v_1\right)\right], \quad (7.9)$$

$$G^{4\beta}_{22} = \left[-\frac{1}{2\phi^0}\left(\phi^0 v_1 T_1 k_\beta + c^{(0)}\phi_1 T_1\right) - \frac{2}{\phi^0 H^2 \mathrm{dim}}k_\beta^2 T_1\left(\kappa^0_\phi\phi_1 + \kappa^0_T T_1\right) + \frac{1}{\phi^0\mathrm{dim}}\left(-k_\beta\left(p^0_\phi\phi_1 + p^0_T T_1\right)v_1 + 2\mu^0 k_\beta^2\left(v_1^2 + \frac{1}{2}u_1^2\right) + \left(\frac{1}{2}\mu^0_{\phi\phi}\phi_1^2 + \frac{1}{2}\mu^0_{TT}T_1^2 + \mu^0_{\phi T}\phi_1 T\right) + 2k_\beta\left(\mu^0_\phi\phi_1 + \mu^0_T T_1\right)u_1 + \lambda^0 k_\beta^2 v_1^2 - \left(\frac{1}{2}\mathscr{D}^0_{\phi\phi}\phi_1^2 + \frac{1}{2}\mathscr{D}^0_{TT}T_1^2 + \mathscr{D}^0_{\phi T}T_1^2\right)\right)\right]. \quad (7.10)$$

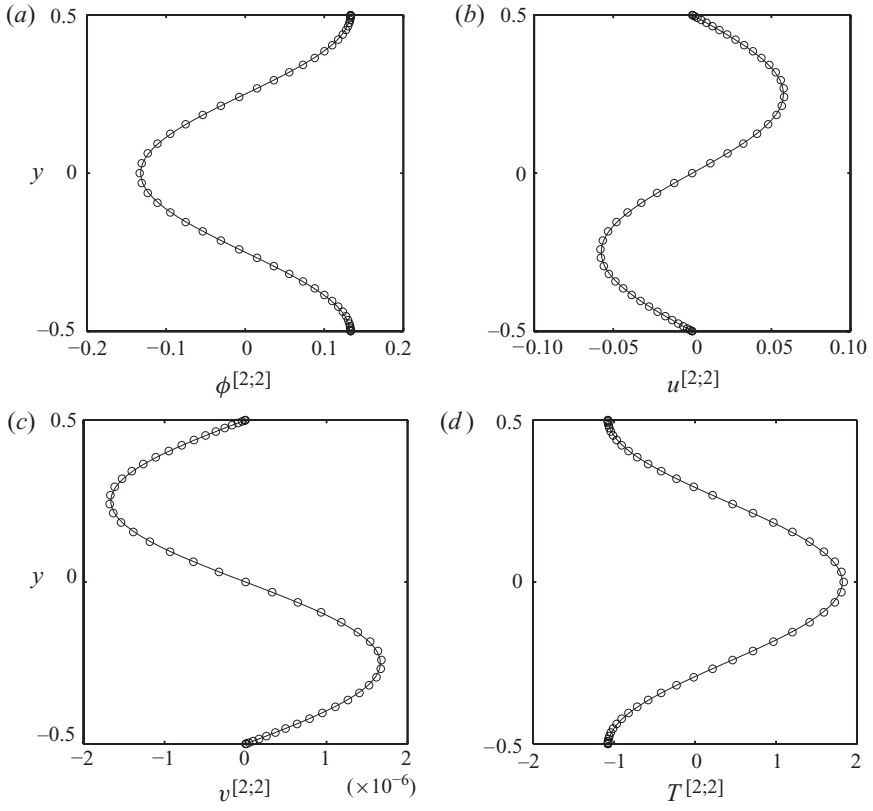

FIGURE 3. Comparison between the analytical (solid line) and spectral/numerical (circles) solutions for the second harmonic $X^{[2;2]}$ with mode $\beta = 1$: (*a*) $\phi^{[2;2]}$, (*b*) $u^{[2;2]}$, (*c*) $v^{[2;2]}$ and (*d*) $T^{[2;2]}$ for $\phi^0 = 0.15$, $H = 100$ and $e = 0.8$.

The matrix equation (7.5) can be easily solved to determine the complete solution for the second harmonic from (7.1).

For the shear-banding mode, the eigenvalue is real (Alam & Nott 1998; Alam *et al.* 2008), i.e. $b^{(0)} = 0$. This implies that

$$\boldsymbol{L}_{22} = \left[2\left(a^{(0)} + \mathrm{i}b^{(0)}\right)\boldsymbol{I} - \boldsymbol{L}\right] = \left[2a^{(0)}\boldsymbol{I} - \boldsymbol{L}\right] \equiv \boldsymbol{L}_{02}, \tag{7.11}$$

i.e. the linear operators for the second harmonic and the mean-flow distortion are identical. From (4.24) and (4.25) we have $G_{22} = N_2(X^{[1:1]}, X^{[1:1]}) = G_{02}$, and therefore

$$X^{[0,2]} = X^{[2,2]} \tag{7.12}$$

for the shear-banding mode. Therefore, the solution to the mean-flow distortion, $X^{[0,2]}$, is the same as in (7.1).

Before moving to the first Landau coefficient, let us compare our analytical solutions for the second harmonic (7.1) with those calculated numerically by discretizing the differential equations using the spectral collocation technique and solving the resulting algebraic equations by the singular value decomposition as detailed in § 6. Figure 3 shows a representative comparison between the analytical and numerical solutions for the shape of the second harmonic for mode $\beta = 1$ at a mean density of $\phi^0 = 0.15$ and $H = 100$. In each panel, the solid line refers to the analytical solution and the

circles to the numerical solution, and we find excellent agreement between the two. It has been verified that a similar level of agreement holds for other modes $\beta = 2, 3, \ldots$.

7.2. *Solution for the first Landau coefficient*

To determine the first Landau coefficient, we consider the equation for the distortion of the fundamental (4.31) which appears at the cubic order. Recall that the inhomogeneous terms G_{13} of this equation depend on the fundamental ($X^{[1,1]}$), the second harmonic ($X^{[2,2]}$) and the mean-flow distortion ($X^{[0,2]}$), along with the base state solution; see (4.32). Inserting solutions for $X^{[1,1]}$, $X^{[2,2]}$ and $X^{[0,2]}$, the expressions of $G_{13} = (G^1_{13}, G^2_{13}, G^3_{13}, G^4_{13})$ are simplified as follows:

$$\left(G^1_{13}, G^4_{13}\right) = 3\left(G^{1\beta3}_{13}, G^{4\beta3}_{13}\right)\cos k_{3\beta}(y \pm 1/2) + 3\left(G^{1\beta1}_{13}, G^{4\beta1}_{13}\right)\cos k_\beta(y \pm 1/2), \quad (7.13)$$

$$\left(G^2_{13}, G^3_{13}\right) = 3\left(G^{2\beta3}_{13}, G^{3\beta3}_{13}\right)\sin k_{3\beta}(y \pm 1/2) + 3\left(G^{2\beta1}_{13}, G^{3\beta1}_{13}\right)\sin k_\beta(y \pm 1/2). \quad (7.14)$$

The y-independent terms $G^{1\beta3}_{13}$, $G^{4\beta3}_{13}$, $G^{1\beta1}_{13}$, $G^{4\beta1}_{13}$, $G^{2\beta3}_{13}$, $G^{3\beta3}_{13}$, $G^{2\beta1}_{13}$ and $G^{3\beta1}_{13}$ are given in Appendix B (Appendix B is part of the supplementary material available at journals.cambridge.org/flm). Inserting G_{13}, $X^\dagger$ and $X^{[1;1]}$ in the numerator and denominator of (4.33), we obtain

$$\begin{aligned}\int_{-1/2}^{1/2} \tilde{X}^\dagger G_{13}\,\mathrm{d}y &= 3\left(\tilde{\phi}^\dagger_1 G^{1\beta3}_{13} + \tilde{T}^\dagger_1 G^{4\beta3}_{13}\right)\int_{-1/2}^{1/2}\cos k_\beta(y \pm 1/2)\cos k_{3\beta}(y \pm 1/2)\,\mathrm{d}y \\ &\quad + 3\left(\tilde{u}^\dagger_1 G^{2\beta3}_{13} + \tilde{v}^\dagger_1 G^{3\beta3}_{13}\right)\int_{-1/2}^{1/2}\sin k_\beta(y \pm 1/2)\sin k_{3\beta}(y \pm 1/2)\,\mathrm{d}y \\ &\quad + 3\left(\tilde{\phi}^\dagger_1 G^{1\beta1}_{13} + \tilde{T}^\dagger_1 G^{4\beta1}_{13}\right)\int_{-1/2}^{1/2}\cos^2 k_\beta(y \pm 1/2)\,\mathrm{d}y \\ &\quad + 3\left(\tilde{u}^\dagger_1 G^{2\beta1}_{13} + \tilde{v}^\dagger_1 G^{3\beta1}_{13}\right)\int_{-1/2}^{1/2}\sin^2 k_\beta(y \pm 1/2)\,\mathrm{d}y \\ &= \frac{3}{2}\left(\tilde{\phi}^\dagger_1 G^{1\beta1}_{13} + \tilde{T}^\dagger_1 G^{4\beta1}_{13} + \tilde{u}^\dagger_1 G^{2\beta1}_{13} + \tilde{v}^\dagger_1 G^{3\beta1}_{13}\right) \quad (7.15)\end{aligned}$$

and

$$\begin{aligned}\int_{-1/2}^{1/2} \tilde{X}^\dagger X^{[1;1]}\,\mathrm{d}y &= \left(\tilde{\phi}^\dagger_1\phi_1 + \tilde{T}^\dagger_1 T_1\right)\int_{-1/2}^{1/2}\cos^2 k_\beta(y \pm 1/2)\,\mathrm{d}y \\ &\quad + \left(\tilde{u}^\dagger_1 u_1 + \tilde{v}^\dagger_1 v_1\right)\int_{-1/2}^{1/2}\sin^2 k_\beta(y \pm 1/2)\,\mathrm{d}y \\ &= \frac{1}{2}\left(\tilde{\phi}^\dagger_1\phi_1 + \tilde{T}^\dagger_1 T_1 + \tilde{u}^\dagger_1 u_1 + \tilde{v}^\dagger_1 v_1\right). \quad (7.16)\end{aligned}$$

The final expression for the first Landau coefficient (4.33) simplifies to

$$c^{(2)} \equiv a^{(2)} + \mathrm{i}b^{(2)} = \frac{3\left(\tilde{\phi}^\dagger_1 G^{1\beta1}_{13} + \tilde{T}^\dagger_1 G^{4\beta1}_{13} + \tilde{u}^\dagger_1 G^{2\beta1}_{13} + \tilde{v}^\dagger_1 G^{3\beta1}_{13}\right)}{\tilde{\phi}^\dagger_1\phi_1 + \tilde{T}^\dagger_1 T_1 + \tilde{u}^\dagger_1 u_1 + \tilde{v}^\dagger_1 v_1}. \quad (7.17)$$

Since for the shear-banding mode the linear eigenfunction, its adjoint and the second harmonic are found to be real, the right-hand side of the above equation is always real for this mode. This implies that the imaginary part of the first Landau coefficient is identically zero for the shear-banding mode:

$$b^{(2)} = 0, \quad \Rightarrow \quad c^{(2)} \equiv a^{(2)}. \quad (7.18)$$

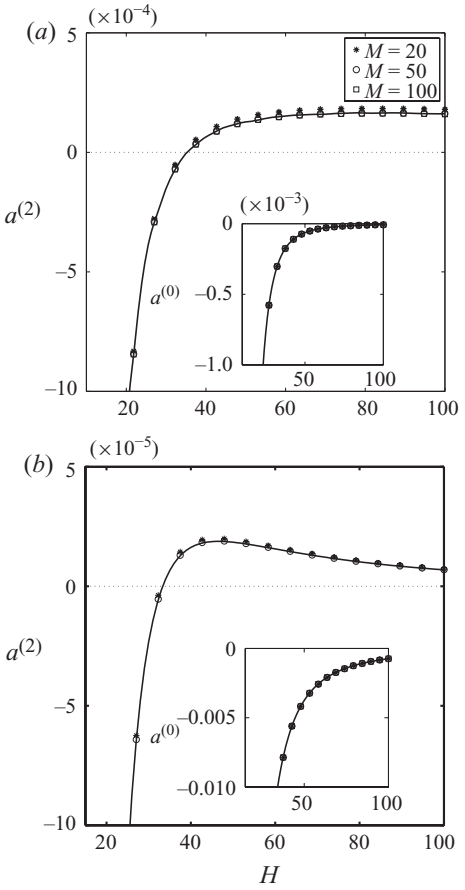

FIGURE 4. Comparison of the first Landau coefficient between the analytical (solid line) and spectral/numerical (the stars, circles and squares correspond to $M = 20$, 50 and 100 collocation points, respectively) solutions: (*a*) $\phi^0 = 0.15$ and (*b*) $\phi^0 = 0.05$, with $e = 0.8$. The inset in each panel shows the variation in the growth rate of the least stable mode (mode number $\beta = 1$) with H.

To compute $a^{(2)}$ analytically, we need to insert the analytical solutions of the fundamental mode (3.13) and the second harmonic (7.1) in (7.17). The solution of the first Landau coefficient from (7.17) is shown in figures 4(*a*) and 4(*b*), shown by solid lines, which display the variations of $a^{(2)}$ with the Couette gap at two values of the mean density $\phi^0 = 0.15$ and 0.05, respectively.

To ascertain the accuracy of the Gauss–Chebyshev quadrature (as detailed in § 6), we also calculated $a^{(2)}$ by using the numerical solutions for the fundamental mode and the second harmonic and then evaluated the integrals in (4.33) by using the Gauss–Chebyshev quadrature with a different number of collocation points (M). The stars, circles and squares in figure 4 denote the corresponding numerical solutions for $a^{(2)}$ with $M = 20$, 50 and 100, respectively, which agree well with our analytical solution. The insets in figures 4(*a*) and 4(*b*) show the variation in the growth rate $a^{(0)}$ of the least stable mode, again calculated both analytically and numerically with excellent agreement between the two. Note that the least stable mode is stable (i.e. $a^{(0)} < 0$) at both mean densities in figure 4, and we will discuss the possibility of subcritical bifurcations in such cases in § 8.3.

The quantitative accuracy of our numerical method was further checked by comparing the numerical values of the least stable growth rate $a^{(0)}$ and the first Landau coefficient $a^{(2)}$ at different parameter values of (ϕ^0, H, e). While $M = 10$ collocation points were found to be sufficient to calculate $a^{(0)}$ within an error of less than 0.001 %, we needed more than $M = 75$ collocation points to calculate $a^{(2)}$ within 1 % error.

7.3. *Solution for higher-order harmonics: distortion of the fundamental mode*

Recall that at cubic order $O(A^3)$ we have two harmonics: the distortion of the fundamental mode $X^{[1;3]}$ and the third harmonic $X^{[3;3]}$. Here we determine an analytical solution for $X^{[1;3]}$. The governing equation for the distortion of the fundamental mode is

$$\boldsymbol{L}_{13} X^{[1;3]} = -c^{(2)} X^{[1;1]} + G_{13}. \tag{7.19}$$

Having determined the first Landau coefficient $c^{(2)} \equiv a^{(2)}$, the right-hand side of (7.19) is now completely known, and hence (7.19) can be solved for $X^{[1;3]}$.

The general solution for $X^{[1;3]}$ for any mode number β can be written as

$$\left.\begin{aligned} \phi^{[1;3]} &= \phi^3_{13} \cos k_{3\beta}(y \pm 1/2) + \phi^1_{13} \cos k_\beta(y \pm 1/2), \\ u^{[1;3]} &= u^3_{13} \sin k_{3\beta}(y \pm 1/2) + u^1_{13} \sin k_\beta(y \pm 1/2), \\ v^{[1;3]} &= v^3_{13} \sin k_{3\beta}(y \pm 1/2) + v^1_{13} \sin k_\beta(y \pm 1/2), \\ T^{[1;3]} &= T^3_{13} \cos k_{3\beta}(y \pm 1/2) + T^1_{13} \cos k_\beta(y \pm 1/2), \end{aligned}\right\} \tag{7.20}$$

where $k_{3\beta} = 3\beta\pi$, with the mode number $\beta = 1, 2, \ldots$, and $[\phi^3_{13}, u^3_{13}, v^3_{13}, T^3_{13}]^{\mathrm{T}}$ and $[\phi^1_{13}, u^1_{13}, v^1_{13}, T^1_{13}]^{\mathrm{T}}$ represent unknown amplitudes. Substituting this solution (7.20) into (7.19) and equating sine and cosine terms, we obtain inhomogeneous algebraic equations for unknown amplitudes that can be easily evaluated.

The analytical solutions (7.20) are compared with the numerical solution of (7.19) in figure 5 at a mean density $\phi^0 = 0.15$. Similar to the second harmonic, we observe good quantitative agreement between the analytical and numerical solutions for each mode shape of $X^{[1;3]}$.

On the whole, the quantitative agreement in figures 3–5 between the analytical and the spectral/numerical solutions for the harmonics (of various orders) of the fundamental mode as well as for the first Landau coefficient ascertains the accuracy of our spectral-based numerical method for nonlinear stability. One outcome of this paper is the validation of a numerical technique (based on the spectral collocation and the Gauss–Chebyshev quadrature) for nonlinear stability calculations: our spectral-based numerical code can be adapted/extended for a host of granular flow problems for which analytical solutions do not exist.

8. Bifurcation, phase diagram and finite-amplitude solution

8.1. *Phase diagram and critical parameters for 'linear' shear-banding instability*

For linear stability, the dispersion relation is a quartic in $c \equiv c^{(0)} = a^{(0)} + \mathrm{i}b^{(0)}$ (Alam & Nott 1998):

$$c^4 + \alpha_3 c^3 + \alpha_2 c^2 + \alpha_1 c + \alpha_0 = 0, \tag{8.1}$$

where α_i are functions of the base state density and temperature, the Couette gap and the restitution coefficient. Previous studies on linear stability (Alam & Nott 1998; Alam *et al.* 2008) have found that out of four eigenvalues of (8.1), there is

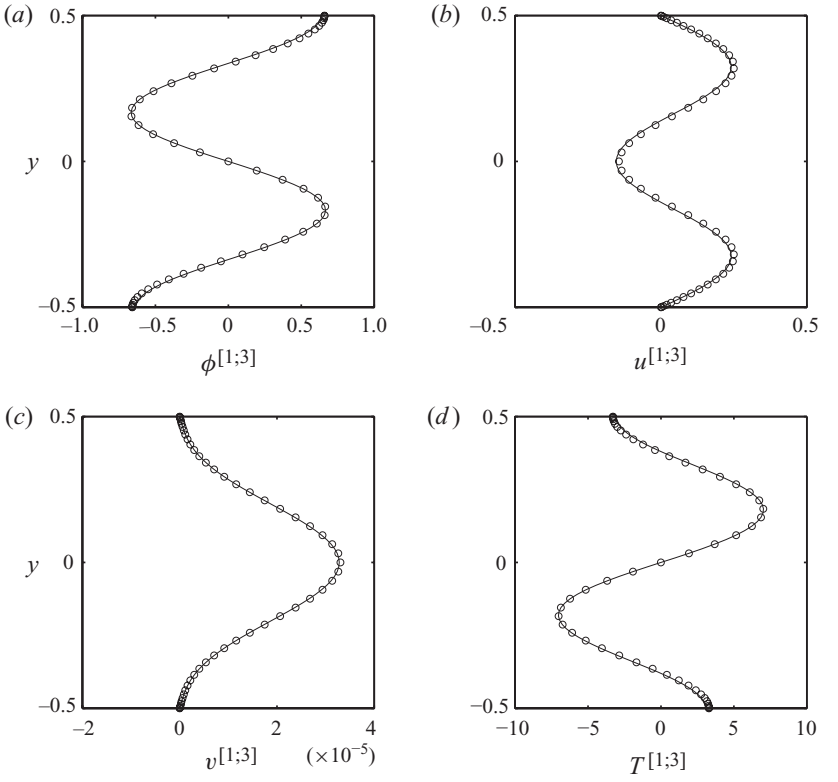

FIGURE 5. Comparison between the analytical (solid line) and spectral/numerical (circles) solutions for the distortion of the fundamental $X^{[1;3]}$ with mode number $\beta = 1$: (*a*) $\phi^{[1;3]}$, (*b*) $u^{[1;3]}$, (*c*) $v^{[1;3]}$ and (*d*) $T^{[1;3]}$. Parameter values are the same as in figure 3.

a complex conjugate pair, representing propagating modes, which is always stable; one real eigenvalue corresponds to the temperature mode which remains the most stable mode for any values of control parameters, and the remaining real eigenvalue could be unstable depending on the base state condition. This real unstable mode has been referred to as the 'shear-banding' mode (Alam 2005) since the corresponding eigenfunctions represent shear localization and density segregation along the gradient (y) direction.

Since the shear-banding instability corresponds to a real eigenvalue, the locus of the neutral stability ($a^{(0)} \equiv \mathrm{Re}(c) = 0$) is given by $\alpha_0 = 0$, which can be simplified to

$$H^2 = \frac{\Psi_1}{\Psi_2} k_\beta^2. \tag{8.2}$$

Here $k_\beta = \beta\pi$, with $\beta = 1, 2, \ldots$ being the mode number, and Ψ_1 and Ψ_2 are functions of the base state density,

$$\Psi_1 = \frac{f_4^0}{f_5^0} \quad \text{and} \quad \Psi_2 = \left(\frac{f_{5\phi}^0}{f_5^0} + \frac{f_{2\phi}^0}{f_2^0} \right) \frac{f_1^0}{f_{1\phi}^0} - 2. \tag{8.3}$$

The zero growth rate contour $a^{(0)} = 0$ (i.e. the neutral stability curve) for the shear-banding mode is shown in figure 6 by a thick solid line; the flow is unstable ($a^{(0)} > 0$) inside the neutral stability contour and stable ($a^{(0)} < 0$) outside. It is seen that for a

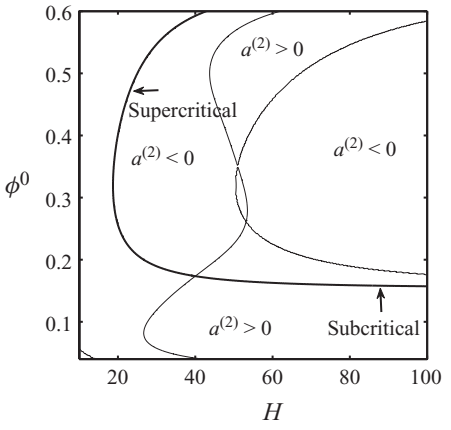

FIGURE 6. Phase diagram in the (H, ϕ)-plane: contours of the zero first Landau coefficient (thin solid lines) and the zero growth rate (thick solid line) in the (H, ϕ^0)-plane for $e = 0.8$ and $\beta = 1$. The flow is unstable ($a^{(0)} > 0$) on the right of the thick solid contour.

given density, there is a minimum/critical value of the Couette gap,

$$H_c = H(\phi^0, e, \beta; a^{(0)} = 0) = k_\beta \sqrt{\Psi_1/\Psi_2}, \tag{8.4}$$

depending on ϕ^0, e and β, below which the shear flow is stable according to linear theory. On the other hand, for a given H, there is a minimum/critical density,

$$\phi_c = \phi^0(H, e, \beta; a^{(0)} = 0), \tag{8.5}$$

below which the shear flow is stable. While this critical density depends on H, e and β, there is a global minimum density, defined as

$$\phi_c^l = \min \phi^0\big(a^{(0)} = 0\big) \quad \forall \quad H, \tag{8.6}$$

below which the uniform shear flow is always stable to the shear-banding instability, irrespective of the values of e and β. For our Navier–Stokes-order model (2.5)–(2.7), this global critical density is $\phi_c^l \approx 0.154$; this numerical value depends on the explicit form of constitutive relations and the radial distribution function as discussed in §§ 9.1 and 9.2.

In the following two sections, we investigate the possibility of subcritical shear-banding instability in dilute flows $\phi^0 < \phi_c^l$ from our nonlinear analysis. One goal is to check the feasibility of finite-amplitude segregated solutions that have been observed in molecular dynamics simulations of the dilute granular shear flow (Tan 1995). This constitutes a stringent test of our order-parameter theory since the same has been predicted from the direct numerical simulation of continuum equations for the same flow configuration (Nott *et al.* 1999). We will also determine finite-amplitude solutions for moderately dense flows ($\phi^0 > \phi_c^l$) which are linearly unstable to shear-banding instability, signalling the possibility of supercritical bifurcations for $\phi^0 > \phi_c^l$.

8.2. *Equilibrium amplitude and the nature of bifurcation*

First we discuss the nature of bifurcation for the appearance of finite-amplitude nonlinear solutions that would bifurcate from the uniform shear base state due to the shear-banding instability as discussed in § 8.1. This is closely tied to the concept

of equilibrium amplitude (i.e. the finite-amplitude equilibrium solution) and the first Landau coefficient $a^{(2)}$ as shown below.

Let us rewrite the amplitude order-parameter or the Landau equation (4.18) as

$$S = \frac{\mathrm{d}A}{\mathrm{d}t} = a^{(0)}A + a^{(2)}A^3 + a^{(4)}A^5 + \cdots, \tag{8.7}$$

which is an infinite series in which $a^{(0)}$ is the growth rate from the linear theory and $a^{(2)}$, $a^{(4)}$, ..., are nonlinear corrections to the linear growth rate, called Landau coefficients. The above series (8.7) is also known as the Stuart–Landau series (Stuart 1960; Watson 1960). As mentioned above, we have restricted ourselves to the leading-order nonlinear correction term by calculating only the first Landau coefficient $a^{(2)}$.

The stationary solution of (8.7), i.e. the value of A for which $S=0$, is called the equilibrium amplitude $A=A_e$. To determine the equilibrium amplitude, we truncate (8.7) at cubic order,

$$\frac{\mathrm{d}A_e}{\mathrm{d}t} = a^{(0)}A_e + a^{(2)}A_e^3 = 0, \tag{8.8}$$

which has three possible solutions:

$$A_e = 0 \quad \text{and} \quad A_e = \pm\sqrt{-\frac{a^{(0)}}{a^{(2)}}}. \tag{8.9}$$

The trivial zero solution, $A_e=0$, corresponds to the base state of the uniform shear, implying that the uniform shear solution is stable if the two non-zero solutions are unfeasible. It is clear that the finite-amplitude/nonlinear solutions exist if and only if the following condition holds:

$$a^{(0)} \quad \text{and} \quad a^{(2)} \text{ are of the opposite sign.}$$

Two situations can arise:

$$\text{(i)} \qquad a^{(0)} > 0 \quad \text{and} \quad a^{(2)} < 0 \qquad \text{(supercritical)}, \tag{8.10}$$

$$\text{(ii)} \qquad a^{(0)} < 0 \quad \text{and} \quad a^{(2)} > 0 \qquad \text{(subcritical)}. \tag{8.11}$$

The former/latter condition corresponds to linearly unstable/stable flow with positive/negative growth rates and negative/positive first Landau coefficients, respectively, leading to supercritical/subcritical bifurcations. In other words, the subcritical bifurcation arises when the first Landau coefficient $a^{(2)}$ has a positive sign and the supercritical bifurcation occurs when $a^{(2)}$ is negative. In either case, there is a new finite-amplitude solution given by (8.9).

8.3. *Phase diagram for 'nonlinear' shear-banding instability*

As described in the previous section, the sign of the first Landau coefficient $a^{(2)}$ decides the type of bifurcation: supercritical (8.10) or subcritical (8.11). From our analytical solution, the condition for the vanishing first Landau coefficient (7.17) simplifies to

$$\tilde{\phi}_1^{\dagger}G_{13}^{1\beta 1} + \tilde{T}_1^{\dagger}G_{13}^{4\beta 1} + \tilde{u}_1^{\dagger}G_{13}^{2\beta 1} + \tilde{v}_1^{\dagger}G_{13}^{3\beta 1} = 0. \tag{8.12}$$

The zero contour of the first Landau coefficient, $c^{(2)}=a^{(2)}=0$, is superimposed over the neutral stability contour ($a^{(0)}=0$) in figure 6 by a thin solid line. The restitution coefficient is set at $e=0.8$, with the mode number being $\beta=1$. The regions of positive and negative $a^{(2)}$ are shown in the figure. Note that the thick solid line in figure 6 corresponds to the zero growth rate contour (i.e. the neutral stability contour), to the

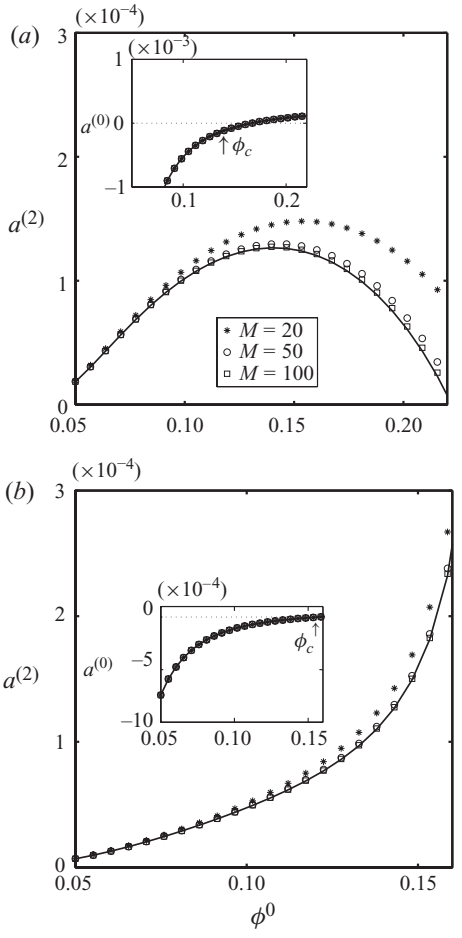

FIGURE 7. Variation of the first Landau coefficient with density for subcritical flows: (*a*) $H = 50$ and (*b*) $H = 100$, with $e = 0.8$. The inset shows the variation in the growth rate of the least stable mode (mode number $\beta = 1$) with density. The solid line represents the analytical solution, and the spectral/numerical solutions are denoted by stars, circles and squares, respectively, with $M = 20$, 50 and 100 collocation points. The arrows in insets show the critical value of density, ϕ_c, above which the flow is linearly unstable (i.e. $a^{(0)} > 0$).

right of which the uniform shear flow is linearly unstable and is stable in the rest of the (ϕ^0, H)-plane.

In the following, we discuss the results of the first Landau coefficient and the related bifurcations for linearly stable ($\phi^0 < \phi_c^l$) and unstable ($\phi^0 > \phi_c^l$) regimes separately in §§ 8.3.1 and 8.3.2, respectively. We will show that the lower part of the neutral contour (enclosed by the zero line of $a^{(2)} = 0$) in figure 6 is subcritically unstable but its upper part is supercritically unstable.

8.3.1. *Linearly stable regime: $\phi^0 < \phi_c^l$*

Focusing on the stable dilute flows ($\phi^0 < \phi_c^l \approx 0.154$) in figure 6, we show the variation of the first Landau coefficient with density in figures 7(*a*) and 7(*b*) for two Couette gaps $H = 50$ and 100, respectively. The inset in each figure shows the corresponding variation in the growth rate of the least stable shear-banding mode ($\beta = 1$); the arrow in each inset shows the critical value of the density, ϕ_c, above

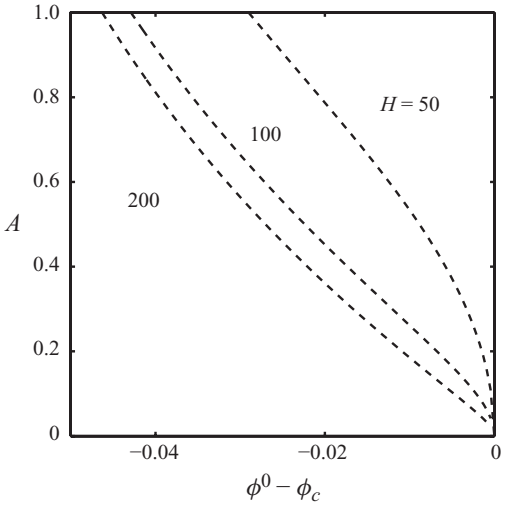

FIGURE 8. Bifurcation diagram in the $(A, \phi^0 - \phi_c)$-plane at three Couette gaps with $e = 0.8$. Note that the bifurcation is subcritical in each case.

which the flow is linearly unstable. For both cases, we find that the growth rate, $a^{(0)}$, is negative but the first Landau coefficient, $a^{(2)}$, is positive for a range of densities in the linearly stable region ($\phi^0 < \phi_c$), suggesting the existence of finite-amplitude solutions as per (8.11). This is also evident from figures 4(a) and 4(b), which show the variations of $a^{(2)}$ (main panel) and $a^{(0)}$ (inset) with the Couette gap at two values of the mean density $\phi^0 < \phi_c^l$.

The bifurcation diagrams in the $(A, \phi^0 - \phi_c)$-plane, related to figures 7(a) and 7(b), are shown in figure 8 for three values of the Couette gap $H = 50$, 100 and 200. For each case, the horizontal line with $A_e = 0$ represents the base state of the uniform shear solution which is stable for $\phi^0 < \phi_c^l$, but we also have new unstable finite-amplitude solutions, representing subcritical bifurcations (also known as inverse bifurcation). For subcritical bifurcations, the higher-order Landau coefficients (which we have not calculated) are needed to identify the stable finite-amplitude solution. Note that the finite-amplitude unstable branch in figure 8 provides a threshold for nonlinear stability: the uniform shear flow is nonlinearly stable/unstable for $A < A_e$ or $A > A_e$, respectively. At a given density, this threshold amplitude A_e, to reach a stable nonlinear state, is higher for smaller Couette gaps. Apart from its dependence on the mean density (ϕ^0) and the Couette gap (H), A_e also depends on the restitution coefficient (e), i.e. $A_e \equiv A_e(\phi^0, H, e)$. This is evident from figure 9, which shows the bifurcation diagrams in the $(A, \phi^0 - \phi_c)$-plane for three values of the restitution coefficient at a Couette gap of $H = 100$. Clearly, the threshold amplitude A_e decreases with increasing dissipation (i.e. with decreasing e).

The results presented in figure 8 can be replotted as a bifurcation diagram in the (A, H)-plane as in figure 10. The mean density is set at $\phi^0 < \phi_c^l = 0.154$ ($\phi^0 = 0.15$ and 0.10 in figures 10a and 10b, respectively) and the restitution coefficient to $e = 0.8$. The finite-amplitude branch in each panel of figure 10 provides a threshold for nonlinear stability, and the magnitude of this nonlinear threshold decreases with increasing Couette gap. In fact, this branch bifurcates from infinity, i.e. from $H = \infty$, as we explain below. Let us consider the leading-order analytical expression for the

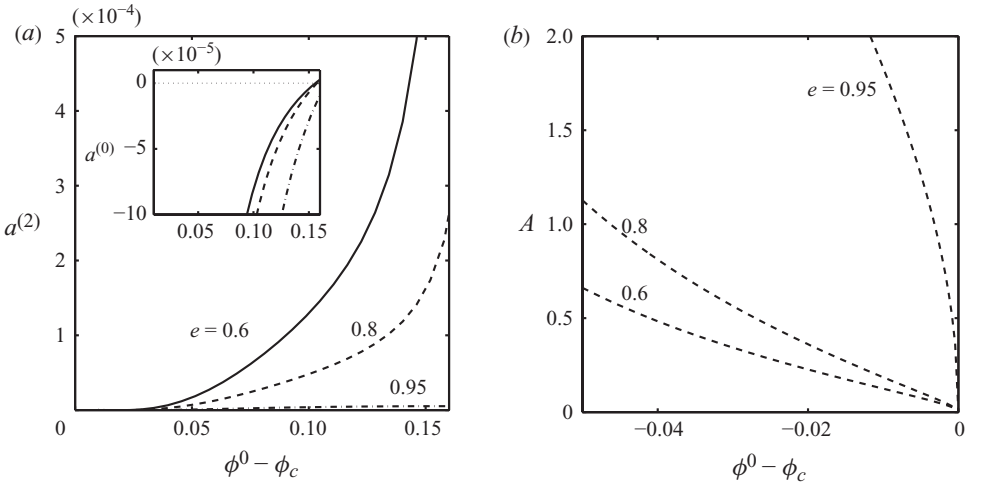

FIGURE 9. Effect of the restitution coefficient on (*a*) the variation of the first Landau coefficient with ϕ^0, and (*b*) the bifurcation diagram in the (A, ϕ^0)-plane for $H = 100$ and $\beta = 1$. The inset shows the related variations in the linear growth rate with ϕ^0 for different e. Note that the bifurcation is subcritical in each case.

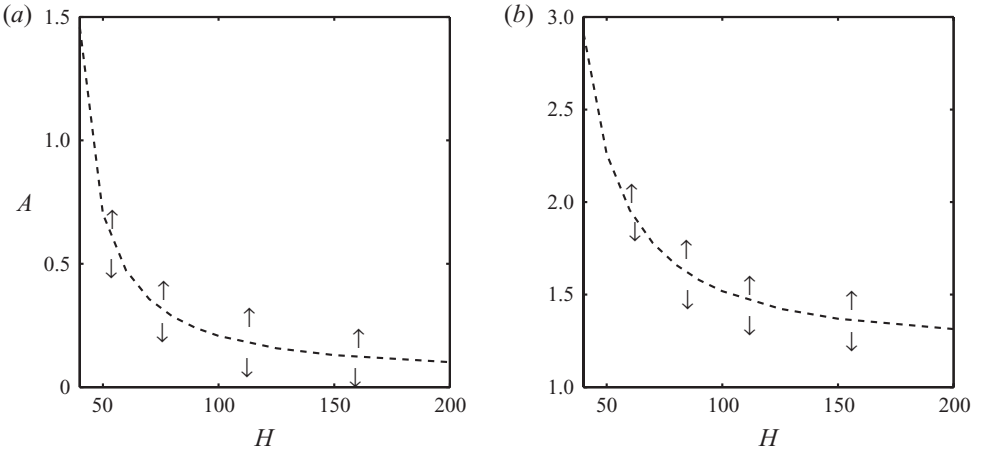

FIGURE 10. Bifurcation from infinity ($H \to \infty$) at (*a*) $\phi^0 = 0.15$ and (*b*) $\phi^0 = 0.1$, with $e = 0.8$.

shear-banding mode (Alam & Nott 1998):

$$a^{(0)} = -H^{-2}\frac{\mu^0\left[p^0_\phi(\mathscr{D}^0_T + \mu^0_T) - p^0_T(\mathscr{D}^0_\phi + \mu^0_\phi)\right]k^2_\beta}{2p^0_T\mu^0 + \phi^0\left[p^0_\phi(\mathscr{D}^0_T - \mu^0_T) - p^0_T(\mathscr{D}^0_\phi - \mu^0_\phi)\right]} + O(H^{-4}). \tag{8.13}$$

It has been verified that $a^{(0)}$ is always negative for $\phi^0 < \phi^l_c$, over which the shear flow is linearly stable. However, it is clear from (8.13) that $a^{(0)} \to 0$ in the limit $H \to \infty$, and hence there is a critical point ($a^{(0)} = 0$) at $H = \infty$. Therefore, the bifurcation point for linearly stable densities ($\phi^0 < \phi^l_c$) originates from $H = \infty$. This is the origin of the nomenclature for the special type of bifurcation as shown in figure 10, bifurcation from infinity (Rosenblat & Davis 1979; Alam 2005). In fact, this belongs to a more general class of subcritical bifurcations.

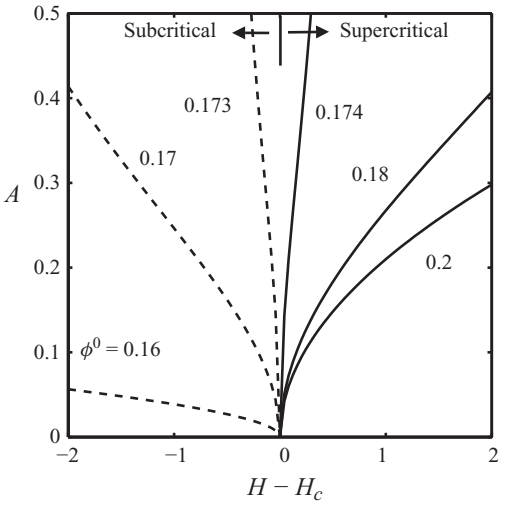

FIGURE 11. Bifurcation diagram in the (A, H)-plane for a range of densities with $e = 0.8$. Note that the bifurcation type changes from supercritical to subcritical below a critical value of the mean density $\phi^0 \in (0.173, 0.174)$.

From the above discussion, we conclude that the region in the (ϕ^0, H)-plane in figure 6, below the intersection of the zero contours of $a^{(2)}$ and $a^{(0)}$, is subcritically unstable. More specifically, in this region $(\phi^0 < \phi_c^l)$ of linearly stable flows, there is a bifurcation from infinity in the sense that the bifurcation point lies at $H = \infty$. In all cases, there exist finite-amplitude nonlinear solutions, provided the amplitude of the perturbation exceeds a threshold for nonlinear stability,

$$A > A_e(\phi^0, H, e), \tag{8.14}$$

which depends on various control parameters.

8.3.2. *Linearly unstable regime: $\phi^0 > \phi_c^l$*

Here we consider moderately dense flows with $\phi^0 > \phi_c^l$, for which the linear stability theory predicts that the uniform shear is unstable to shear-banding instability if the Couette gap is sufficiently large; more specifically, we focus on the regime in figure 6 which is enclosed by the neutral stability contour $(a^{(0)} = 0)$.

Figure 11 shows a series of bifurcation diagrams in the $(A, H - H_c)$-plane for six values of the mean density, $\phi^0 = 0.16$, 0.17, 0.173, 0.174, 0.18 and 0.2, just above the critical density for the onset of the linear shear-banding instability. The restitution coefficient is set at $e = 0.8$, as in figure 6. It is clear that the bifurcation type is not supercritical immediately, even though we are in the linearly unstable regime $(\phi^0 > \phi_c^l)$. However, we have a window of mean densities,

$$\phi_c^l \leqslant \phi^0 \leqslant \phi_c^s, \tag{8.15}$$

with $\phi_c^s \in (0.173, 0.174)$, over which the bifurcation is subcritical and is supercritical for larger densities,

$$\phi^0 > \phi_c^s. \tag{8.16}$$

From figure 11 we find that the critical density at which this switchover between the subcritical and supercritical bifurcations occurs is about $\phi_c^s \approx 0.1735$.

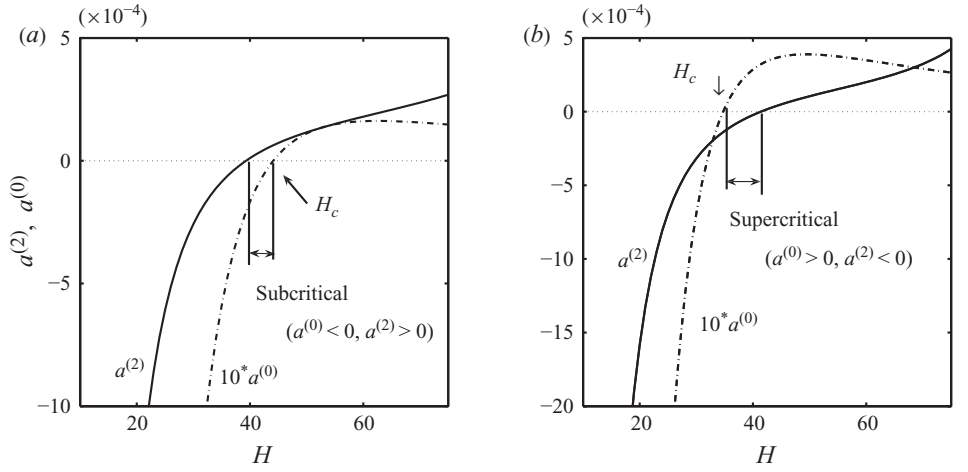

FIGURE 12. Variations in the first Landau coefficient, $a^{(2)}$, and the growth rate of the least stable shear-banding mode, $a^{(0)}$, with the Couette gap for linearly unstable mean densities $\phi^0 > \phi_c^l \approx 0.154$: (*a*) $\phi^0 = 0.17$ and (*b*) 0.18. The arrow in each panel shows the critical Couette gap H_c, above which the shear flow is linearly unstable ($a^{(0)} > 0$).

To understand the origin of the above switchover between the two bifurcations, we show the variation of the first Landau coefficient with H at $\phi^0 = 0.17$ and 0.18 in figures 12(*a*) and 12(*b*), respectively. In each figure, we have superimposed the corresponding variation of the least stable mode, $a^{(0)}$, shown by the dot-dashed line, and the critical Couette gap, $H_c = H(a^{(0)} = 0)$, is also shown by an arrow. In the case of $\phi^0 = 0.17 < \phi_c^s$, we find a range of Couette gaps (shown by vertical lines in figure 12*a*) over which $a^{(0)} < 0$ and $a^{(2)} > 0$, which correspond to subcritical bifurcations (8.11). On the other hand, for $\phi^0 = 0.18 > \phi_c^s$, we have a range of Couette gaps (shown by vertical lines in figure 12*b*) over which $a^{(0)} > 0$ and $a^{(2)} < 0$, signalling the presence of supercritical bifurcations (8.10).

Even at larger mean densities ($\phi^0 \gg \phi_c^s$), the bifurcation remains supercritical as seen in figure 13(*a*). The corresponding variations of $a^{(2)}$ and $a^{(0)}$ are shown in the main panel and the inset of figure 13(*b*). At both $\phi^0 = 0.3$ and 0.5, the condition for the supercritical bifurcation (8.10), $a^{(0)} > 0$ and $a^{(2)} < 0$, is satisfied. It is seen from figure 13(*a*) that the magnitude of A, required to reach the nonlinear finite-amplitude branch, increases with increasing density.

In § 9, we will discuss the possible influence of different constitutive relations and the contact radial distribution function on the above bifurcation scenario.

8.4. *Finite-amplitude solutions: density segregation and shear localization*

Once we know the equilibrium amplitude, the finite-amplitude solutions for the density and the shear rate are computed from

$$\phi = \phi^0 \pm A_e \phi^{[1:1]}, \tag{8.17}$$

$$\gamma = \frac{\mathrm{d}}{\mathrm{d}y}\left(u^0 \pm A_e u^{[1:1]}\right), \tag{8.18}$$

with leading-order corrections in the amplitude $O(A)$. Typical subcritical finite amplitude solutions for ϕ and γ are shown in figures 14(*a*) and 14(*b*), respectively, for mode $\beta = 1$, with parameter values $\phi^0 = 0.15$, $H = 100$ and $e = 0.8$. The analogue of these figures for mode $\beta = 2$ is shown in figures 15(*a*) and 15(*b*). For any mode number

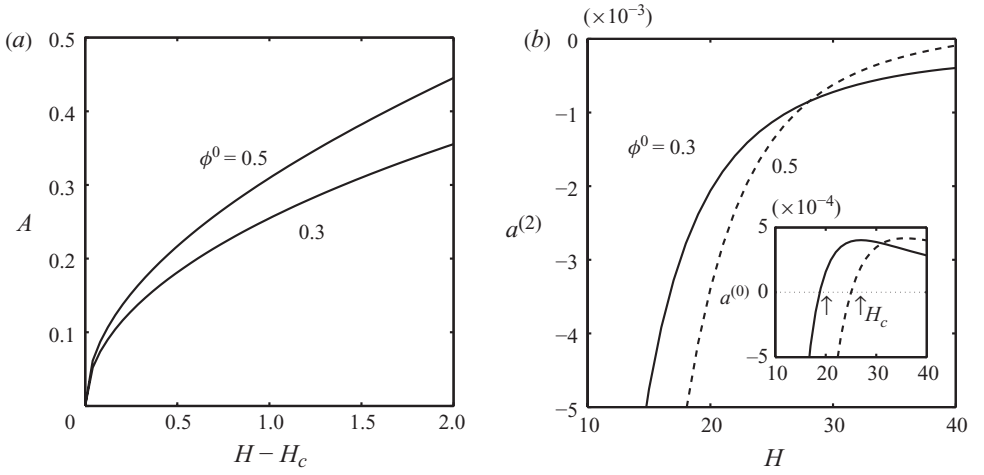

FIGURE 13. (*a*) Bifurcation diagrams in the (A, H)-plane and (*b*) the variations of first Landau coefficients at larger mean densities, $\phi^0 \gg \phi_c^l$, with $e = 0.8$. The inset shows the variations in the linear growth rate with H.

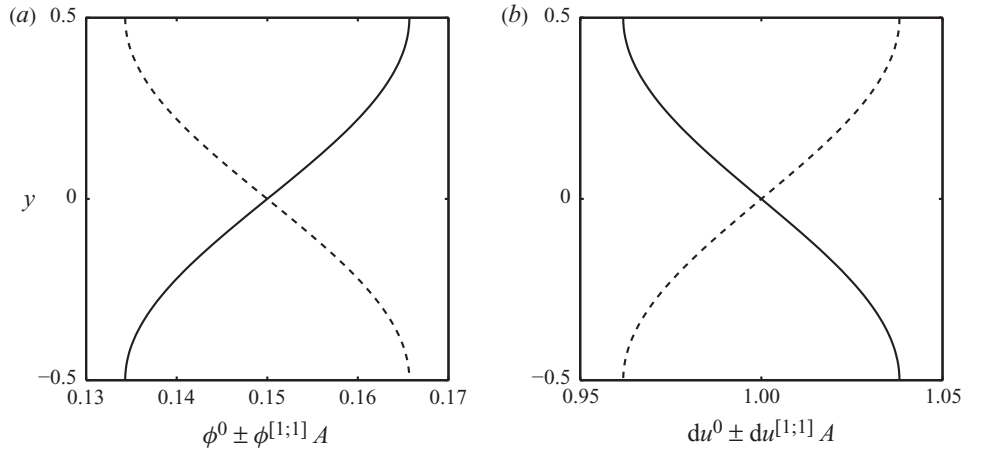

FIGURE 14. Finite-amplitude solutions for (*a*) the density, $\phi^0 + A\phi^{[1;1]}$ and (*b*) the shear rate, $\mathrm{d}/\mathrm{d}y(u^0 + Au^{[1;1]})$, for mode $\beta = 1$. Parameter values are $\phi^0 = 0.15$, $H = 100$ and $e = 0.8$

β, there are two solutions that are mirror-symmetric, which is due to the underlying symmetry of the plane Couette flow. It is clear that the density and shear rate are non-uniform across the Couette gap (y), leading to density segregation and shear localization – the shear rate is large/small in the dilute/dense regions, respectively. The varying shear rate across the Couette gap (i.e. along the gradient direction) is the hallmark of shear-banded solutions in complex fluids (Olmsted 2008). Note that the solution profiles shown in figures 14 and 15 are 'unstable' since they belong to the unstable 'subcritical' bifurcation branch. For subcritical bifurcations, the higher-order Landau coefficients (which we have not calculated) are needed to identify stable finite-amplitude solutions. The 'stable' finite-amplitude solutions of the density and the shear rate, corresponding to supercritical bifurcations (for example, at $\phi^0 = 0.3$

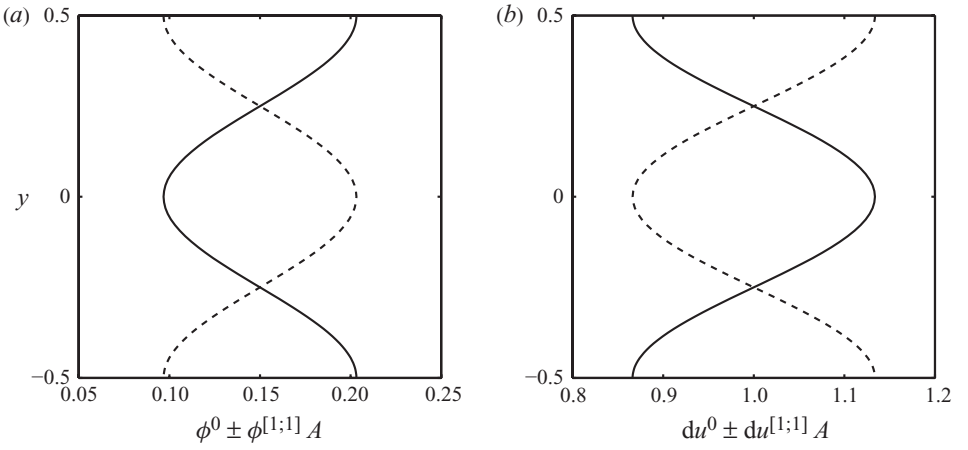

FIGURE 15. Same as figure 14, but for mode $\beta = 2$.

and $H > H_c$, as in figure 13*a*), are also characterized by shear localization and density segregation across the gradient direction, similar to those shown in figures 14 and 15.

8.5. *Scaling of the first Landau coefficient, equilibrium amplitude and bifurcation diagram*

So far we have presented bifurcation diagrams and the first Landau coefficients for mode $\beta = 1$. In this section, we will demonstrate that there exists a simple scaling for $a^{(0)}$, $a^{(2)}$ and A in terms of mode number β with respect to the Couette gap H. More specifically, we will show that the dependencies of $a^{(0)}$, $a^{(2)}$ and A (at a given density ϕ^0) on β can be absorbed by defining a new length scale: $H \to H^*(H, \beta)$. In other words, knowing the variations of $a^{(0)}$, $a^{(2)}$ and A with H for any β (at a given density), one can determine these quantities at other values of β at the same mean density. (However, there is no such scaling solution in terms of mean density.) We will further demonstrate that the phase diagrams in the (H, ϕ^0)-plane, showing zero loci of $a^{(2)}$ and $a^{(0)}$, remain invariant under a composite scaling for the Couette gap: $H \to H^*(H, \beta, e)$, i.e. in terms of both β and the inelasticity $(1 - e^2)$.

Figure 16(*a*) shows the effect of mode number β on the first Landau coefficient $a^{(2)}$ (main figure) and the linear mode $a^{(0)}$ (inset) for parameter values of $\phi^0 = 0.3$ and $e = 0.8$. The flow becomes unstable to higher-order modes at larger values of the Couette gap; see the inset of figure 16(*a*). The corresponding supercritical bifurcation diagrams for $\beta = 1$, 2 and 3 are shown in figure 16(*b*) – note that the abscissa has been normalized via $H - H_c$, where $H_c = H_c(\beta)$ is the critical Couette gap, as denoted by vertical arrows in the inset of figure 16(*a*). When the Couette gap is rescaled via $H \to H/\beta$, the results for various β do collapse on a single curve for each case of $a^{(2)}$ (main panel of figure 17*a*), $a^{(0)}$ (inset of figure 17*a*) and A (figure 17*b*).

The above scaling of the equilibrium amplitude with β also holds for subcritical values of the mean density; see figures 18(*a*) and 18(*b*) for $\phi^0 = 0.15$ and 0.1, respectively. The inset in each figure displays the variations of A with H for three values of $\beta = 1, 2, 3$. Such scaling of A with H/β holds at any value of the restitution coefficient (not shown).

It has been verified (not shown for brevity) that the scaling of the Couette gap in terms of mode number, $H \to H/\beta$, holds for the zero contours of the first Landau coefficient $a^{(2)} = 0$ in the entire (H, ϕ^0)-plane at any value of the restitution

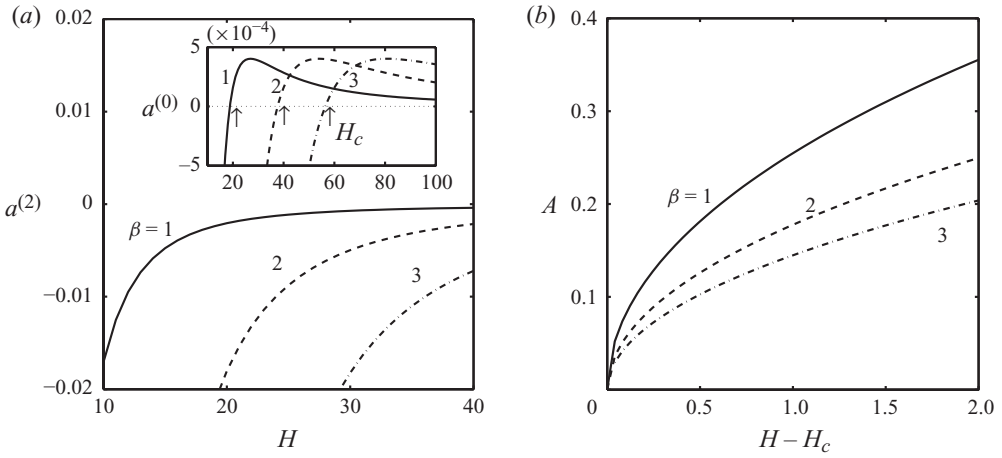

FIGURE 16. Effects of the mode number β on the (a) variation of $a^{(2)}$ and $a^{(0)}$ and (b) the bifurcation diagram in the (A, H)-plane. Parameter values are $\phi^0 = 0.3$ and $e = 0.8$.

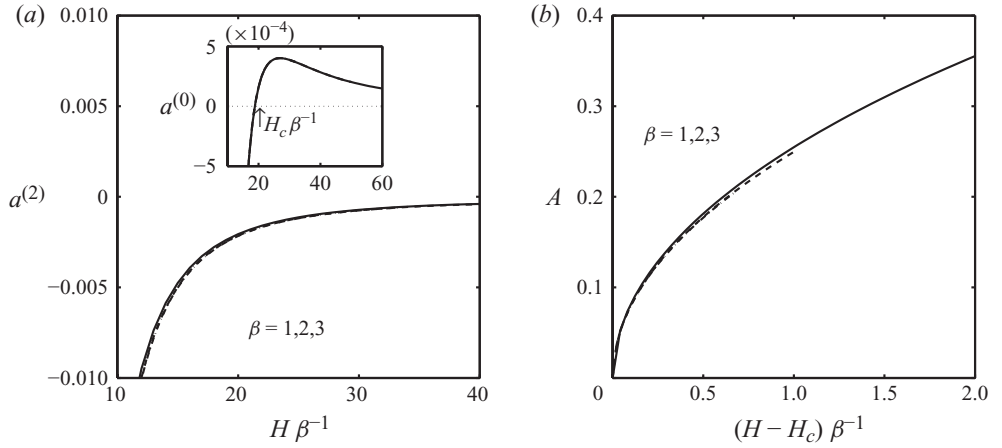

FIGURE 17. Universal scaling with β of the variations of (a) $a^{(2)}$ and $a^{(0)}$ and (b) A with H. Parameter values are $\phi^0 = 0.3$ and $e = 0.8$.

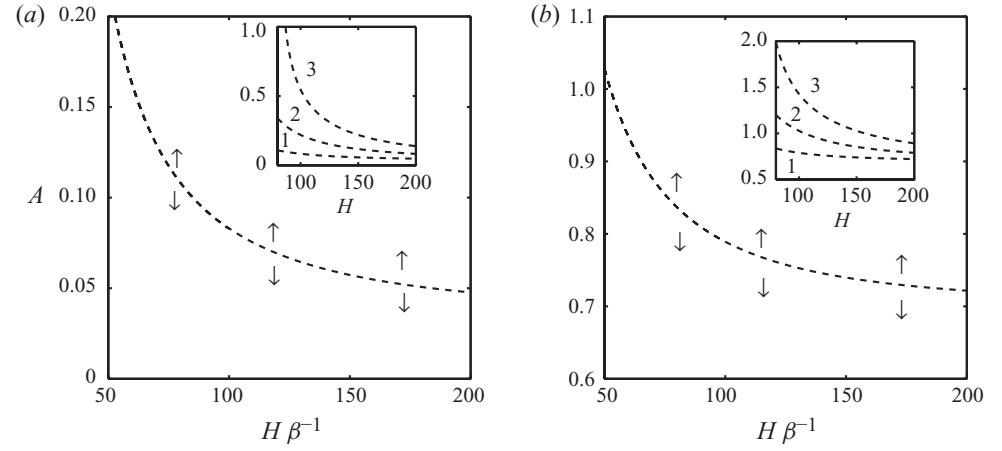

FIGURE 18. Bifurcation from infinity: (a) $\phi^0 = 0.15$ and (b) $\phi^0 = 0.1$ at $e = 0.6$.

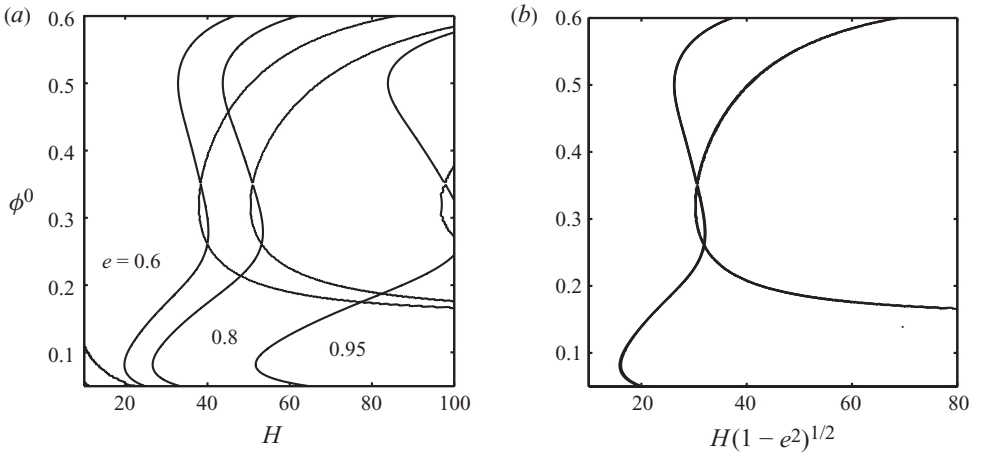

FIGURE 19. Scaling for the zero contour of the first Landau coefficient, $a^{(2)} = 0$, in terms of the restitution coefficient for mode $\beta = 1$.

coefficient e. Furthermore, the phase diagrams also remain invariant under a simple transformation in terms of inelasticity: $H \to H\sqrt{1-e^2}$, see figure 19. Three sets of contours of $a^{(2)} = 0$ in the (H, ϕ^0)-plane for $e = 0.95$, 0.8 and 0.6 (figure 19*a*) collapse onto a single contour as seen in figure 19(*b*) when the horizontal axis is scaled by $H \to H\sqrt{1-e^2}$.

For the neutral stability contour $[a^{(0)} = 0]$, the above-mentioned composite length scale, $H^*(H, e, \beta)$, directly arises from the analysis of our linear stability results. From (8.4) we find that the locus of the neutral stability contour $(a^{(0)} = 0)$ is given by $H \sim \beta\sqrt{\psi_1} \sim \beta(1-e^2)^{-1/2}$ since $\psi_1 \sim 1/f_5^0 \sim (1-e^2)^{-1}$; see (8.3). Therefore, the neutral stability contour, $a^{(0)} = 0$, would remain invariant under the following scaling of the Couette gap:

$$H \to H\beta^{-1}\sqrt{(1-e^2)} \equiv H^*. \tag{8.19}$$

It is still not clear why the above composite scaling (8.19) should hold for the zero contour of the first Landau coefficient $a^{(2)} = 0$. The expression for $a^{(2)} = 0$ in (8.12) can be simplified to (see (C9) in Appendix C, part of the supplementary material available at journals/.cambridge.org/flm)

$$H^2 = \frac{-\left(k_\beta^4 K_1 + k_\beta^3 K_2 + k_\beta^2 K_3 + k_\beta K_4\right)}{\left(k_\beta^3 K_5 + k_\beta^2 K_6 + k_\beta K_7 + K_0\right)}, \tag{8.20}$$

where $k_\beta = \pi\beta$ and the expressions for $K_1, K_2, K_3, \ldots$, which depend on base state variables (and hence on the restitution coefficient e) as well as on the modal amplitudes of the fundamental and second harmonic, are given in Appendix C. The dependence of K_i on β comes via the implicit dependence of modal amplitudes on β and hence not known *a priori*. Nevertheless, it appears that the same composite scaling for the Couette gap (8.19) also holds for the zero loci of the first Landau coefficient, as demonstrated in figure 19.

Finally, figure 20 displays the scaled phase diagram in the (H^*, ϕ^0)-plane, where $H^* = H\beta^{-1}\sqrt{(1-e^2)}$ is a new length scale or an instability length scale, delineating the regions of the supercritical and subcritical bifurcations. The grey-shaded region in figure 20 corresponds to $a^{(2)} > 0$ and $a^{(0)} > 0$ and, therefore, no finite-amplitude solution is possible at cubic order, according to (8.9), in the shaded region. There

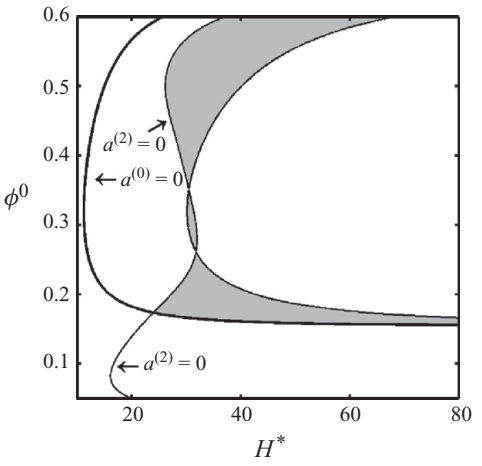

FIGURE 20. Scaled phase diagrams in the (H^*, ϕ^0)-plane, where $H^* = H\beta^{-1}\sqrt{(1-e^2)}$, showing the zero contours of the first Landau coefficient, $a^{(2)} = 0$, and the linear growth rate $a^{(0)} = 0$. The shaded region corresponds to $a^{(2)} > 0$ and $a^{(0)} > 0$.

is subcritical bifurcation in the dilute limit (below the lower branch of the neutral contour and on the right of the $a^{(2)} = 0$ contour), and supercritical bifurcation at moderate-to-large densities.

9. Discussion

9.1. *Influence of radial distribution function*

So far we have presented results for a specific choice of the contact radial distribution function, $\chi(\phi)$, as defined in (2.7), which was chosen following the linear stability analysis of Alam & Nott (1998). Here, we consider a modified form of the well-known Carnahan–Starling radial distribution function, $\chi(\phi)$:

$$\chi(\phi) = \frac{(1 - \phi/2)}{(1 - \phi/\phi_m)^3}, \tag{9.1}$$

where ϕ_m corresponds to the maximum solid fraction at a random close packing which is taken to be 0.65 in the present work. Note that with $\phi_m = 1$, (9.1) reduces to the well-known Carnahan–Starling form with its singularity being at $\phi_m = 1$, which corresponds to point particles.

With constitutive relations as in (2.5)–(2.6) and the Carnahan–Starling radial distribution function (9.1), we show the scaled phase diagram in the (H^*, ϕ^0)-plane, where $H^* = H\beta^{-1}\sqrt{(1-e^2)}$ and ϕ^0 is the mean density, in figure 21(*a*) for $\phi_m = 0.65$. (The overall features of the phase diagram remain similar at other values of ϕ_m.) The thick solid line is the neutral stability contour ($a^{(0)} = 0$), to the right of which the flow is linearly unstable and is stable outside; the thin lines correspond to the zeros of the first Landau coefficient $a^{(2)} = 0$. A contrasting feature between the phase diagram in figure 21(*a*) and that in figure 20 (for which we had used (2.7) as the radial distribution function) is that the zero contour of the first Landau coefficient $a^{(2)} = 0$ crosses the neutral stability curve $a^{(0)} = 0$ at two additional points at large densities in the former. Recall that a crossing of $a^{(2)} = 0$ and $a^{(0)} = 0$ signals a switchover from one type of bifurcation to another. This is clearly shown in the bifurcation diagrams in the (H^*, A)-plane in figure 21(*c*,*d*), with parameter values as in figure 21(*a*). In

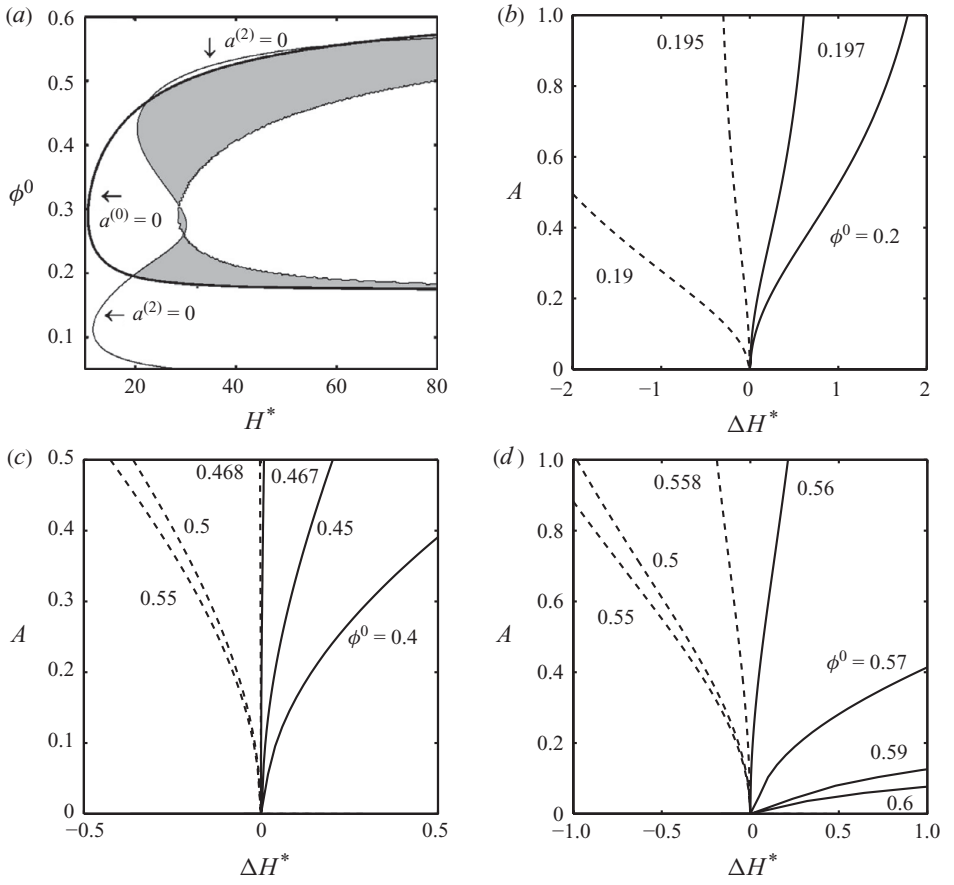

FIGURE 21. (*a*) Scaled phase diagram in the (H^*, ϕ^0)-plane, where $H^* = H\beta^{-1}\sqrt{(1-e^2)}$, showing the zero contours of the first Landau coefficient, $a^{(2)}=0$, and the linear growth rate $a^{(0)}=0$. The shaded region corresponds to $a^{(2)}>0$ and $a^{(0)}>0$. Constitutive relations are the same as in figure 20 (as in § 2.1), except that we used the Carnahan–Starling radial distribution (9.1) with $\phi_m = 0.65$. (*b–d*) Bifurcation diagrams in the $(A, \Delta H^*)$-plane, where $\Delta H^* = H^* - H_c^*$, showing a sequence of transitions from subcritical to supercritical bifurcations and vice versa; see text for details.

figure 21(*c*,*d*), a series of finite-amplitude bifurcating solutions are shown against $\triangle H^* = H^* - H_c^*$ (i.e. a renormalized Couette gap) that measures a distance from its respective neutral/critical point ($H^* = H_c^*$, with H_c as defined in (8.4)). It is clear that the nature of bifurcation changes (from subcritical to supercritical or vice versa) with increasing mean density in each figure. We find three critical densities at which the nature of bifurcation changes: (i) from subcritical to supercritical bifurcations at $\phi_c^s \approx 0.196$, in figure 21(*b*); (ii) from supercritical to subcritical bifurcations at $\phi_c^s \approx 0.467$, in figure 21(*c*); and (iii) from subcritical to supercritical bifurcations at $\phi_c^s \approx 0.559$, in figure 21(*d*). While the first transition from subcritical to supercritical bifurcation was also found for the radial distribution function (2.7), the last two transitions in the dense limit, supercritical → subcritical → supercritical, are specific to the choice of the Carnahan–Starling-type radial distribution function (9.1).

We conclude that both the radial distribution functions, (2.7) and (9.1), predict a similar bifurcation scenario (bifurcation-from-infinity → subcritical →

supercritical) at dilute-to-moderate densities; however, the Carnahan–Starling-type radial distribution function (9.1) is responsible for the onset of subcritical bifurcations in the dense limit. Clearly, the exact form of the radial distribution function is needed to correctly predict the bifurcation type (sub- or supercritical) and the corresponding critical density for the onset of the nonlinear shear-banding instability.

9.2. *Influence of constitutive relations: disks versus spheres*

Recall that the constitutive expressions for $f_i(.)$ values (dimensionless functions of the solid fraction, ϕ) in (2.6), which were used in all calculations, are valid only for spheres. Therefore, our results pertain to the granular plane Couette flow in two dimensions, having a monolayer of spheres along the spanwise direction. It is interesting to ascertain whether our predictions about the onset of the nonlinear shear-banding instability and the corresponding bifurcation scenario in different density regimes still hold if we use constitutive relations for hard disks.

For hard disks in two dimensions (dim = 2), the balance equations and the form of constitutive relations remain unaltered; however, the expressions for $f_i(.)$ values as defined in (2.6) are different for disks:

$$\left.\begin{aligned} f_1(\phi) &= \phi(1+2\phi\chi), \\ f_2(\phi) &= \frac{\sqrt{\pi}}{8\chi} + \frac{\sqrt{\pi}}{4}\phi + \frac{\sqrt{\pi}}{8}\left(1+\frac{8}{\pi}\right)\phi^2\chi, \\ f_3(\phi) &= \frac{2}{\sqrt{\pi}}\phi^2\chi, \\ f_4(\phi) &= \frac{\sqrt{\pi}}{2\chi} + \frac{3\sqrt{\pi}}{2}\phi + \sqrt{\pi}\left(\frac{2}{\pi}+\frac{9}{8}\right)\phi^2\chi, \\ f_5(\phi, e) &= \frac{4}{\sqrt{\pi}}(1-e^2)\phi^2\chi. \end{aligned}\right\} \tag{9.2}$$

In two dimensions, the contact radial distribution function, $\chi(\phi)$, is chosen to be of the form

$$\chi(\phi) = \frac{(1-7\phi/16)}{(1-\phi/\phi_m)^2}, \tag{9.3}$$

which diverges at $\phi = \phi_m$, which is taken to be either (i) $\phi_m = \pi/2\sqrt{3} \approx 0.906$ (the maximum packing limit in two dimensions) or (ii) $\phi_m = \phi_r \approx 0.82$ (the random close packing limit in two dimensions). The expression (9.3) reduces to that of Henderson for $\phi_m = 1$, which corresponds to point particles.

Recall that changing the explicit forms of constitutive relations amounts to changing only the forms of the linear and nonlinear operators, $\boldsymbol{L}_{kn}$ and G_{kn}, respectively, in (4.20) since the governing equations (2.1)–(2.4) and the boundary conditions (2.8) are the same for both spheres and disks. With constitutive relations (9.2) and (9.3), we have repeated some of the nonlinear stability calculations that we briefly discuss here. The scaled phase diagram in the (H^*, ϕ^0)-plane, where $H^* = H\beta^{-1}\sqrt{(1-e^2)}$ and ϕ^0 is the mean density, is shown in figure 22(a) for $\phi_m = 0.906$. A closer look at the zero contour of the first Landau coefficient $a^{(2)} = 0$ and the neutral contour $a^{(0)} = 0$ near the dense limit (at much larger values of $H^* \sim 500$) ascertains that there is no crossover between $a^{(2)} = 0$ and $a^{(0)} = 0$, except that at a moderate density $\phi^0 \sim 0.37$. With parameter values as in figure 22(a), a series of bifurcation diagrams in the $(A, \triangle H^*)$-plane are shown in figure 22(b) for a range of mean densities. For this case, the nature of bifurcation changes from subcritical to supercritical at $\phi_c^s \approx 0.373$.

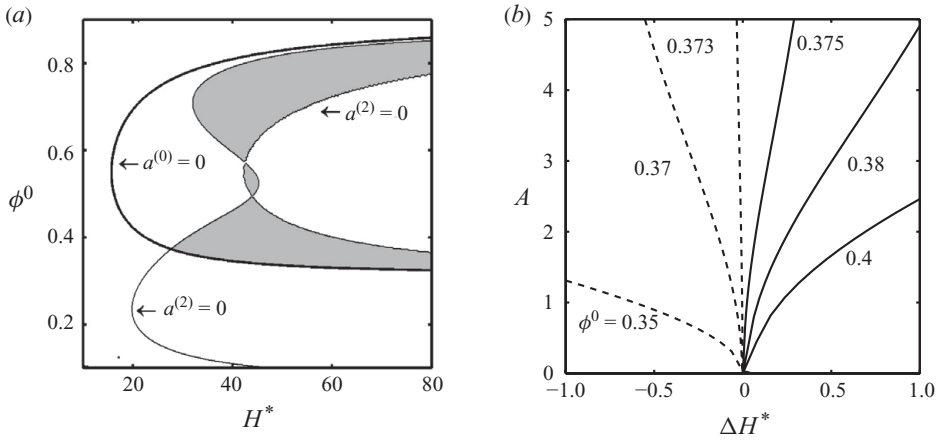

FIGURE 22. (*a*) Scaled phase diagram in the (H^*, ϕ^0)-plane, where $H^* = H\beta^{-1}\sqrt{(1-e^2)}$, for constitutive relations for hard disks (two dimensions) as in (9.2)–(9.3) with $\phi_m = \pi/2\sqrt{3} \approx 0.906$. (*b*) Bifurcation diagrams in the $(A, \Delta H^*)$-plane, where $\Delta H^* = H^* - H_c^*$, showing a transition from subcritical to supercritical bifurcations.

Note in figure 22(*a*) that the flow is linearly stable in the dilute limit, and the shear-banding occurs via a 'bifurcation-from-infinity' for $\phi_c^l \leqslant 0.338$. A comparison between figures 22(*a*) and 20 reveals that the region of 'bifurcation-from-infinity' is much larger for hard disks.

With constitutive expressions for hard disks as in (9.2) and (9.3), the following sequence of pitchfork bifurcations, leading to nonlinear shear-banded solutions, holds as we increase the mean density from the Boltzmann limit: bifurcation-from-infinity → subcritical → supercritical. In contrast to results for spheres, we do not find subcritical bifurcations in the dense limit for hard disks with (9.2) and (9.3). We have verified that the same sequence of bifurcations also holds even if we allow the shear viscosity to diverge at a faster rate than other transport coefficients.

9.3. *Granular plane Couette flow as a 'microcosm' of pitchfork bifurcations*

Let us now summarize our results on different types of pitchfork bifurcations in the granular plane Couette flow that result from the nonlinear saturation of the shear-banding instability. With (2.7) as the contact radial distribution function and the constitutive relations as in § 2.1, the sequence of pitchfork bifurcations in the present flow configuration, with increasing mean density, reads as

$$\left.\begin{aligned} \text{bifurcation from infinity:} \quad & \phi^0 < \phi_c^l \approx 0.154, \\ \text{subcritical bifurcation:} \quad & \phi_c^l < \phi^0 < \phi_c^s, \\ \text{supercritical bifurcation:} \quad & \phi^0 > \phi_c^s \approx 0.1735. \end{aligned}\right\} \tag{9.4}$$

This prediction is the same as in our previous paper, Shukla & Alam (2009). Note that the direct numerical simulation of continuum equations (2.1)–(2.4) for the same problem (Nott *et al.* 1999) has also identified the above three types of bifurcations. By changing the contact radial distribution function to the Carnahan–Starling type (9.1), with $\phi_m = 0.65$, and the constitutive relations as in § 2.1, the sequence of pitchfork

bifurcations reads as

$$\left.\begin{aligned}
\text{bifurcation from infinity:}\quad & \phi^0 < \phi_c^l \approx 0.174,\\
\text{subcritical bifurcation:}\quad & \phi_c^l < \phi^0 < \phi_c^s \approx 0.196,\\
\text{supercritical bifurcation:}\quad & \phi_c^s < \phi^0 < \phi_c^{s1} \approx 0.467,\\
\text{subcritical bifurcation:}\quad & \phi_c^{s1} < \phi^0 < \phi_c^{s2} \approx 0.559,\\
\text{supercritical bifurcation:}\quad & \phi^0 > \phi_c^{s2}.
\end{aligned}\right\} \tag{9.5}$$

This bifurcation sequence remains intact even when the singularity of the Carnahan–Starling radial distribution function (9.1) is moved to $\phi_m = 1$; only the critical densities at which each transition occurs are quantitatively different: $\phi_c^l \approx 0.218$, $\phi_c^s \approx 0.246$, $\phi_c^{s1} \approx 0.717$ and $\phi_c^{s2} \approx 0.842$.

It is clear from the above discussion that the sequence of bifurcations (the first three in (9.4) and (9.5)) remains the same in the regime of dilute to moderate densities, irrespective of explicit forms of constitutive relations for different transport coefficients; however, the nature of bifurcations at larger densities (especially the appearance of subcritical bifurcations in the dense limit) depends crucially on constitutive relations and the contact radial distribution function. It is recommended to employ the exact forms of constitutive relations that are likely to be valid in the whole range of densities (which can be obtained from particle simulations) so as to make a fair conclusion about the bifurcation type and the corresponding critical density for the onset of the nonlinear shear-banding instability in the granular plane Couette flow. Such a detailed parametric study is beyond the scope of the present paper and is left to the future.

Figure 23 summarizes all possible bifurcation scenarios for the nonlinear shear-banding instability in a granular plane Couette flow. Note that a single control parameter, the mean density (ϕ^0), needs to be varied to obtain any type of pitchfork bifurcation in this flow. Therefore, the granular plane Couette flow serves as a microcosm of pitchfork bifurcations since all three possible types of pitchfork bifurcations, as shown schematically in figure 23, can be realized by just varying the mean density.

Moving to the well-researched field of Newtonian fluids, we note that a similar type of bifurcation from infinity occurs in the plane Couette flow (Nagata 1990); note, however, that there is no supercritical or subcritical bifurcations in this flow since the Newtonian plane Couette flow is known to be stable according to the linear stability theory (Romanov 1973). For Newtonian fluids, the examples of subcritical and supercritical bifurcations can be found in the plane Poiseuille flow (Stuart 1960; Reynolds & Potter 1967) and Rayleigh–Bénard convection (Busse 1978), respectively. We are not aware of any flow which admits all three types of pitchfork bifurcations and, therefore, the granular plane Couette flow is truly a paradigm for pitchfork bifurcations.

9.4. *Qualitative comparison with particle simulations and experiment*

The plethora of pitchfork bifurcations in the granular plane Couette flow, as summarized in figure 23, agrees qualitatively with previous particle simulations of the same flow (Tan 1995; Tan & Goldhirsch 1997; Sasvari, Kertesz & Wolf 2000; Alam & Luding 2003; Conway & Glasser 2004; Conway, Liu & Glasser 2006; Khain & Meerson 2006; Saitoh & Hayakawa 2007; Khain 2007). For example, the earliest simulations of Tan (1995) with inelastic hard disks in the dilute regime (at a particle volume fraction of 0.05) identified shear-banding patterns with a dense plug around

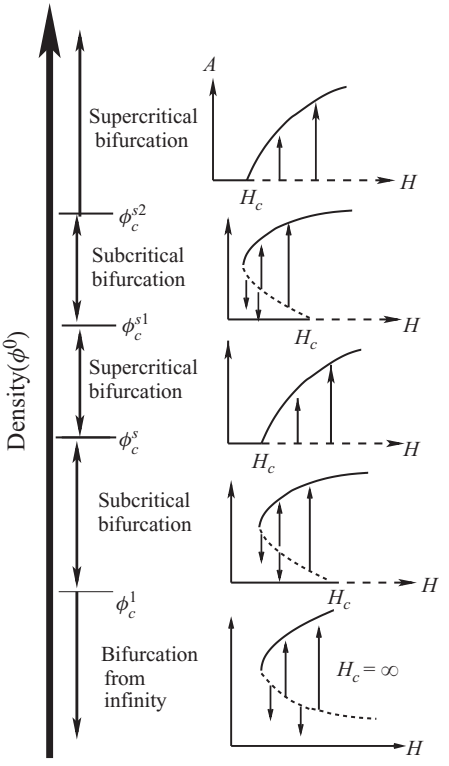

FIGURE 23. A schematic of different types of pitchfork bifurcations, showing the whole paradigm, in the granular plane Couette flow. The dashed lines in the subcritical bifurcation diagrams represent threshold amplitude for nonlinear stability.

the channel centreline and the corresponding density profile is similar to that in figure 15(*a*), denoted by the dashed line. As discussed previously (Shukla & Alam 2009), the related bifurcation scenario corresponds to the 'bifurcation-from-infinity' (at $\phi^0 < \phi_c^l$ as in figure 23) – our order-parameter theory resolved a related paradox, 'the appearance of shear-bands in a linearly stable flow', by providing a threshold perturbation amplitude which is likely to trigger nonlinearly stable shear-banding patterns even in a 'dilute' granular plane Couette flow (which is stable according to the linear stability theory). As for the latter point, the overall bifurcation scenario predicted by our order-parameter theory is also in tune with previous direct numerical simulations of the same hydrodynamic equations (Nott *et al.* 1999). Therefore, the shear-banding in the granular plane Couette flow is an instability-induced-ordering phenomenon.

The inelastic hard disk simulations of the bounded shear flow at a particle volume fraction of 0.3 by Sasvari *et al.* (2000) showed that the 'asymmetric' shear-banding patterns with a dense plug located near one of the walls can be sustained in a plane Couette flow. According to our order-parameter theory, such asymmetric shear-bands can appear due to pitchfork bifurcations from odd-modes $\beta = 1, 3, \ldots$, with typical density profiles as in figure 14(*a*) for mode $\beta = 1$. Alam & Luding (2003) have also identified such asymmetric shear-bands in dense flows, as well as the recent simulations of Khain (2007). Khain (2007) further showed that even in the dense regime of the plane Couette flow, the shear-bands can appear via a 'hysteretic' transition (i.e. a subcritical bifurcation and hence bistability) – this agrees with our predictions of

subcritical bifurcations in the dense limit at $\phi_c^{s1} < \phi^0 < \phi_c^{s2}$ (see figure 23). Note that Khain (2007) compared his simulation results with the numerical solution of Navier–Stokes-order hydrodynamic equations with a set of modified constitutive relations, with reasonable agreement between the two. Conway & Glasser (2004) and Conway *et al.* (2006) have conducted large-scale particle simulations of the granular plane Couette flow of both monodisperse and bidisperse particles. They found the existence of 'stable' symmetric and asymmetric shear-bands (with the symmetry being about the spatial location of the shear-band around the channel centreline) for a range of particle volume fractions spanning from the dilute to the dense regime. All these simulation results agree qualitatively with our order-parameter theory, which predicts both symmetric and asymmetric shear-banding modes which can be stable/unstable depending on the Couette gap and inelasticity.

The experimental evidence of shear-bands in the 'rapid' shear regime has been lacking since the plane Couette flow is hard to realize in Earth-bound experiments where gravity dominates, leading to a collapsed state near the bottom wall. However, the recent experiments by Conway *et al.* (2006) in a circular Couette geometry at very high shear rates have uncovered the possible existence of shear-bands. Note that only a monolayer of glass beads resting on a bottom glass plate and confined within an annular gap of about 65 particle diameters was sheared by rotating the inner cylinder at very high speeds, which was varied up to a maximum shear rate of 221 s^{-1}. The novelty in these experiments was that the bottom wall of the Couette cell had a mild inward slope (less than 5°) to mitigate the effect of the centrifugal force. Above a shear rate of about 44 s^{-1}, the particles formed a single dense plug (of about 15 particle diameters width) located around the centreline of the annular cell away from both walls, and the resulting pattern was shown to be stable over the experimental time scales of 30 min. The measurement of the instantaneous velocity field using particle image velocimetry confirmed that the shear rate is large within the particle-lean regions and small within the particle-rich (plug) regions, signalling the onset of shear-banding-type patterns. Clearly, more such careful experiments or those under microgravity conditions are required to quantitatively verify the theoretical and simulation results. In summary, it is fair to conclude from the above discussion that the order-parameter theory, the simulation and the experiment agree qualitatively with regard to the formation of shear-bands in the rapid granular plane Couette flow.

10. Conclusions and outlook

We have analysed the nonlinear stability of the granular plane Couette flow, focusing on the shear-banding instability (Alam & Nott 1998; Alam 2005; Alam *et al.* 2008) for which the shear flow degenerates into an ordered state with shear localization and density segregation along the gradient direction. The amplitude expansion method of Stuart and others (Stuart 1960; Watson 1960; Reynolds & Potter 1967) has been adapted to the present nonlinear problem of the streamwise-independent granular plane Couette flow. Using this perturbation method, the nonlinear stability problem has been reduced to a sequence of linear inhomogeneous differential equations for the fundamental mode (linear eigenfunction) and its harmonics and the related distortions of the base flow and the fundamental mode at various orders. The amplitude expansion method constitutes an indirect method to arrive at the Landau equation, and the related nonlinear corrections, the Landau coefficients, are determined from the Fredholm alternative or the solvability condition at the cubic/higher order in the perturbation amplitude.

While the amplitude expansion method is physically appealing and easy to adapt, as we have shown in this paper, the present method differs from several direct methods of nonlinear stability analysis (e.g. the centre-manifold reduction, Carr 1981, Shukla & Alam 2009; multiple scale analysis, Stewartson & Stuart 1971), wherein the Landau equation is derived directly from the nonlinear perturbation equations, which is in contrast to the present method where the order-parameter equation is postulated based on physical arguments about the possible time evolution of the linear mode. In the case of the centre-manifold reduction, the nonlinear analysis is carried out through a spectral decomposition of the fast and slow modes (Shukla & Alam 2009); the relevant order-parameter equation is derived by taking the inner product of the evolution equation of the slow mode with its adjoint eigenfunction and the Landau coefficients are subsequently picked up from the coefficients of nonlinear terms of various orders. We have shown that both the direct and indirect methods lead to the same expression for the first Landau coefficient, which is the first nonlinear correction to the well-studied linear theory. Therefore, up to the first Landau coefficient, both the amplitude expansion method and the centre-manifold reduction are equivalent to the present problem of the granular Couette flow. The development of an order-parameter theory for the shear-banding instability in the granular Couette flow, using the amplitude expansion method, and establishing its equivalence with the centre-manifold reduction constitute the first major outcome of the present paper.

For the shear-banding instability, the nonlinear modes are found to follow certain symmetries of the fundamental mode and the base state solution, which have helped us to discover analytical solutions for the second harmonic and the distortion of the fundamental mode. It is shown that the second harmonic and the base state distortion at the quadratic order are equal to each other for this instability. The present analytical solutions for nonlinear modes have been used to evaluate the first Landau coefficient exactly, which complements and verifies our previous numerical solution of the same problem (Shukla & Alam 2009). These analytical solutions further helped to identify universal scalings for the first Landau coefficient, the equilibrium amplitude, and the phase diagram in the (H, ϕ^0)-plane in terms of the mode number β and the inelasticity $(1-e^2)^{1/2}$, as detailed in § 8.5. Uncovering the analytical solution for the nonlinear shear-banding instability in the granular plane Couette flow constitutes the second major outcome of this paper.

Concurrently, we have developed a numerical method, based on the Chebyshev spectral collocation technique, to solve the inhomogeneous differential equations at each order in the perturbation amplitude. The quantitative agreement between our analytical and the spectral solutions for the fundamental mode and its harmonics (of various orders), as well as for the first Landau coefficient, ascertains the accuracy of our spectral-based numerical method. This constitutes the third major outcome of this paper: the validation of a numerical scheme for nonlinear stability calculations, via its comparison with our analytical solutions, which can now be adapted to other types of granular shear flows.

Analysing the zero contour of the first Landau coefficient in the (H, ϕ^0)-plane, where $H = \overline{h}/\overline{d}$ is the ratio between the Couette gap $(\overline{h})$ and the particle diameter $(\overline{d})$ and ϕ^0 is the mean volume fraction of particles, we have re-established our previous prediction (Shukla & Alam 2009) that the lower branch of the neutral stability curve (i.e. the 'zero' growth rate contour) in the (H, ϕ^0)-plane is subcritically unstable. The related threshold amplitude for the nonlinear stability has been determined, leading to the possibility of shear-banding-type solutions in dilute flows via subcritical bifurcations. In contrast to the predictions of the nonlinear theory, the dilute flows are known to be

stable to gradient banding according to the linear stability theory (Alam & Nott 1998; Alam *et al.* 2008). Irrespective of the nature of bifurcation, the predicted nonlinear solutions indicate that the uniform shear flow undergoes an ordering transition into alternate layers of dense and dilute regions of low and high shear rates, respectively, along the gradient direction (and hence the name 'gradient banding').

Our order-parameter theory predicts that the nonlinear shear-banding instability leads to different types of pitchfork bifurcations (see figure 23) as we increase the mean density (ϕ^0) from the Boltzmann limit: (i) bifurcation from infinity in the Boltzmann limit ($\phi^0 < \phi_c^l$), (ii) subcritical bifurcations over a small window of moderate densities ($\phi_c^l < \phi^0 < \phi_c^s$), (iii) supercritical bifurcations at moderate densities ($\phi_c^s < \phi^0 < \phi_c^{s1}$), (iv) subcritical bifurcations in the dense limit ($\phi_c^{s1} < \phi^0 < \phi_c^{s2}$), and finally again to (v) supercritical bifurcations near the close packing limit ($\phi^0 > \phi_c^{s2} \sim \phi_m$). Note that the 'bifurcation from infinity' can be considered as a generalized subcritical bifurcation wherein the bifurcation point originates from infinity ($H = \infty$). The critical density at which a transition occurs from one bifurcation type to another (ϕ_c^l, ϕ_c^s, ϕ_c^{s1} and ϕ_c^{s2}) depends on the detailed forms of constitutive relations as well as on the choice of the contact radial distribution function. We have found that while the first three sequences of bifurcations (i–iii) appear to be independent of the choice of constitutive relations, the last two bifurcation sequences (iv–v), especially the appearance of subcritical bifurcations in the dense limit, depend on the choice of the contact radial distribution function. Since all three possible types of pitchfork bifurcations can be realized in this flow by just varying the mean density, we conclude that the granular plane Couette flow truly serves as a microcosm of pitchfork bifurcations. The predicted bifurcation scenario for the shear-band formation and the structure of hydrodynamic fields are found to be in qualitative agreement with particle dynamics simulations and experiment in the rapid shear regime of the granular Couette flow as discussed in § 9.4.

Although we have focused on streamwise-independent flows (i.e. one-dimensional) in this paper, our analysis is in no way limited but can be extended to analyse patterns in the two- and three-dimensional plane Couette flows (Shukla & Alam 2010); for example, we could allow inhomogeneities along both the streamwise and spanwise directions, leading to spatially extended patterns for which a similar order-parameter theory can be developed. Our spectral-based numerical code can be adapted to such cases to analyse the nonlinear stability in a host of granular flow problems for which analytical solutions would be hard to come by: granular Faraday waves (Umbanhower *et al.* 1996; Tsimring & Aranson 1997), granular Rayleigh–Bénard convection (Hayakawa, Yue & Hong 1995; Eshuis *et al.* 2010), granular Poiseuille flow (Raafat, Hulin & Herrmann 1996; Alam, Chikkadi & Gupta 2009) and inclined chute flow (Forterre & Pouliquen 2002). To investigate these flows using the present order-parameter theory, we need to incorporate realistic boundary conditions (i.e. the slip velocity and non-adiabatic walls), which are beyond the scope of this paper.

In weakly nonlinear stability studies, one important issue is the convergence of the Stuart–Landau series (4.18)–(4.19), which can be checked by determining its radius of convergence provided we know higher-order (second, third, etc.) Landau coefficients. Such studies have been carried out for incompressible shear flows of Newtonian fluids (Herbert 1980; Newell *et al.* 1993) by calculating the first 10 or more Landau coefficients, and then finding the nearest singularity from Domb–Sykes plots (Hinch 1991) to estimate the radius of convergence. For the present problem of the granular Couette flow, we have calculated only the first Landau coefficient and, therefore, we are unable to make any conclusion about the range of validity of our nonlinear

solutions in the parameter space (away from the neutral contour). Moreover, we need to calculate at least the second Landau coefficient to determine the stable solution branches for subcritical bifurcations. In principle, the higher-order Landau coefficients can be calculated; however, the related analysis and algebra become messy and tedious due to the nonlinearities inherent in the transport coefficients of granular fluids. Such an exercise would further help to establish a detailed term-by-term equivalence between the amplitude expansion method and the centre-manifold reduction for the granular plane Couette flow. These issues should be looked into in future.

We acknowledge partial funding support from a project (BARC/MA/4216). We dedicate this paper to Professor Vijay H. Arakeri on the occasion of his 65th birthday and to the memory of late Professor Isaac Goldhirsch, who passed away on 29 April 2010 while this paper was under review.

Supplementary data are available at journals.cambridge.org/flm.

Appendix A. Nonlinear terms $\mathscr{N}_2$ and $\mathscr{N}_3$

(Appendix A is available at journals.cambridge.org/flm)

Appendix B. Inhomogeneous terms G_{13}

(Appendix B is available at journals.cambridge.org/flm)

Appendix C. Locus of $a^{(2)} = 0$

(Appendix C is available at journals.cambridge.org.flm)

REFERENCES

Alam, M. 2005 Universal unfolding of pitchfork bifurcations and the shear-band formation in rapid granular Couette flow. In *Trends in Applications of Mathematics to Mechanics* (ed. Y. Wang & K. Hutter), pp. 11–20. Shaker.

Alam, M., Arakeri, V. H., Goddard, J., Nott, P. R. & Herrmann, H. J. 2005 Instability-induced ordering, universal unfolding and the role of gravity in granular Couette flow. *J. Fluid Mech.* **523**, 277.

Alam, M., Chikkadi, V. K. & Gupta, V. K. 2009 Density waves and the effect of wall roughness in granular Poiseuille flow: simulation and linear stability. *Eur. Phys. J.. ST*, **179**, 69.

Alam, M. & Luding, S. 2003 First normal stress difference and crystallization in a dense sheared granular fluid. *Phys. Fluids* **15**, 2298.

Alam, M. & Luding, S. 2005 Energy nonequipartition, rheology and microstructure in sheared bidisperse granular mixtures. *Phys. Fluids* **17**, 063303.

Alam, M. & Nott, P. R. 1998 Stability of plane Couette flow of a granular material. *J. Fluid Mech.* **377**, 99.

Alam, M., Shukla, P. & Luding, S. 2008 Universality of shearbanding instability and crystallization in sheared granular fluid. *J. Fluid Mech.* **615**, 293.

Aranson, I. S. & Kramer, L. 2002 The world of the complex Ginzburg–Landau equation. *Rev. Mod. Phys.* **74**, 99.

Aranson, I. S. & Tsimring, L. S. 2006 Patterns and collective behaviour in granular media: theoretical concepts. *Rev. Mod. Phys.* **78**, 641.

Berret, J.-F., Porte, G. & Decruppe, J.-P. 1997 Inhomogeneous shear flows of wormlike micelles: a master dynamic phase diagram. *Phys. Rev.* E **55**, 1668.

Bonn, D., Meunier, J., Greffier, O., Al-Kahwaji, A. & Kellay, H. 1998 Bistability in non-Newtonian flow: rheology and lyotropic liquid crystals. *Phys. Rev.* E **58**, 2115.

Brey, J. J., Santos, A. & Dufty, J. W. 1998 Kinetic models for granular flow. *J. Stat. Phys.* **97**, 281.

Brilliantov, N. & Pöschel, T. 2004 *Kinetic Theory of Granular Gases*. Oxford University Press.

Busse, F. H. 1978 Nonlinear properties of thermal convection. *Rep. Prog. Phys.* **41**, 1929.

Canuto, C., Hussaini, M. Y., Quarteroni, A. & Zang, T. A. 1988 *Spectral Methods in Fluid Dynamics*. Springer.

Carr, J. 1981 *Applications of Center Manifold Theory*. Springer.

Caserta, S., Simeon, M. & Guido, S. 2008 Shearbanding in biphasic liquid–liquid systems. *Phys. Rev. Lett.* **100**, 137801.

Chikkadi, V. K. & Alam, M. 2009 Slip velocity and stresses in granular Poiseuille flow via event-driven simulation. *Phys. Rev.* E **80**, 021303.

Conway, S. & Glasser, B. J. 2004 Density waves and coherent structures in granular Couette flow. *Phys. Fluids* **16**, 509.

Conway, S., Liu, X. & Glasser, B. J. 2006 Instability-induced clustering and segregation in high-shear Couette flows of model granular materials. *Chem. Engng Sci.* **64**, 6404.

Cross, M. C. & Hohenberg, I. 1993 Pattern formation outside of equilibrium. *Rev. Mod. Phys.* **65**, 851.

Eshuis, P., van der Meer, D., Alam, M., van Gerner, H. J., van der Welle, K. & Lohse, D. 2010 Onset convection in strongly shaken granular matter. *Phys. Rev. Lett.* **104**, 038001.

Fornberg, B. 1998 *A Practical Guide to Pseudospectral Methods*. Cambridge University Press.

Forterre, F. & Pouliquen, O. 2002 Stability analysis of rapid granular chute flows: formation of longitudinal vortices. *J. Fluid Mech.* **467**, 361.

Garzo, V. & Dufty, J. W. 1999 Dense fluid transport for inelastic hard spheres. *Phys. Rev.* E **59**, 5895.

Gayen, B. & Alam, M. 2006 Algebraic and exponential instabilities in a sheared micropolar granular fluid. *J. Fluid Mech.* **567**, 195.

Goldhirsch, I. 2003 Rapid granular flows. *Annu. Rev. Fluid Mech.* **35**, 267.

Greco, F. & Ball, R. 1997 Shear-band formation in a non-Newtonian fluid model with constitutive instability. *J. Non-Newton. Fluid Mech.* **69**, 195.

Hanifi, A., Schmid, P. J. & Henningson, D. S. 1996 Transient growth in compressible boundary layer flow. *Phys. Fluids* **8**, 826.

Hayakawa, H., Yue, S. & Hong, D. C. 1995 Hydrodynamic description of granular convection. *Phys. Rev. Lett.* **75**, 2328.

Herbert, T. 1980 Nonlinear stability of parallel flows by high-order amplitude expansions. *AIAA J.* **18**, 243.

Hinch, E. J. 1991 *Perturbation Methods*. Cambridge University Press.

Hoffman, R. L. 1972 Discontinuous and dilatant viscosity behaviour in concentrated suspensions. Part I. Observation of a flow instability. *Trans. Soc. Rheol.* **16**, 155.

Khain, E. 2007 Hydrodynamics of fluid–solid coexistence in dense shear granular flow. *Phys. Rev.* E **75**, 051310.

Khain, E. & Meerson, B. 2006 Shear-induced crystallization of a dense rapid granular flow: hydrodynamics beyond the melting point. *Phys. Rev.* E **73**, 061301.

Lettinga, M. P. & Dhont, J. K. G. 2004 Non-equilibrium phase behaviour of rodlike viruses under shear flow. *J. Phys. Cond. Matter* **16**, S3929.

Lun, C. K. K., Savage, S. B., Jeffrey, D. J. & Chepurniy, N. 1984 Kinetic theories for granular flow: inelastic particles in Couette flow and slightly inelastic particles. *J. Fluid Mech.* **140**, 223.

Malik, M., Dey, J. & Alam, M. 2008 Linear stability, transient energy growth and the role of viscosity stratification in compressible plane Couette flow. *Phys. Rev.* E **77**, 036322.

Manneville, P. 1990 *Dissipative Structures and Weak Turbulence*. Academic Press.

Mueth, D. M., Debregeas, G. F., Karczmar, G. S., Eng, P. J., Nagel, S. & Jaeger, H. J. 2000 Signatures of granular microstructure in dense shear flows. *Nature* **406**, 385.

Nagata, M. 1990 Three-dimensional finite-amplitude solutions in plane Couette flow: bifurcation from infinity. *J. Fluid Mech.* **217**, 519.

Newell, A. C., Passot, T. & Lega, J. 1993 Order parameter equations for patterns. *Annu. Rev. Fluid Mech.* **25**, 399.

Nott, P. R., Alam, M., Agrawal, K., Jackson, R. & Sundaresan, S. 1999 The effect of boundaries on the plane Couette flow of granular materials: a bifurcation analysis. *J. Fluid Mech.* **397**, 203.

Olmsted, P. D. 2008 Perspective on shear banding in complex fluids. *Rheol. Acta* **47**, 283.

Press, W. H., Teukolsky, S. A., Vellerling, W. T. & Flannery, B. P. 1992 *Numerical Recipes*. Cambridge University Press.

Raafat, T., Hulin, J. P. & Herrmann, H. J. 1996 Density waves in dry granular media falling through a vertical pipe. *Phys. Rev.* E **53**, 4345.

Reynolds, W. C. & Potter, M. C. 1967 Finite amplitude instability of parallel shear flows. *J. Fluid Mech.* **27**, 465.

Romanov, J. 1973 Stability of incompressible plane Couette flow. *J. Funct. Anal.* **37**, 1.

Rosenblat, S. & Davis, S. H. 1979 Bifurcation from infinity. *SIAM J. Appl. Math.* **37**, 1.

Saitoh, K. & Hayakawa, H. 2007 Rheology of a granular gas under a plane shear flow. *Phys. Rev.* E **75**, 021302.

Sasvari, M., Kertesz, Y. & Wolf, D. E. 2000 Instability of symmetric granular Couette flow in a granular gas: hydrodynamic field profiles and transport. *Phys. Rev.* E **62**, 3817.

Savage, S. B. & Sayed, S. 1984 Stresses developed by dry cohesionless granular materials sheared in an annular shear cell. *J. Fluid Mech.* **142**, 391.

Schall, P. & van Hecke, M. 2010 Shear bands in matter with granularity. *Annu. Rev. Fluid Mech.* **42**, 67.

Sela, N. & Goldhirsch, I. 1998 Hydrodynamic equations for rapid shear flows of smooth, inelastic spheres, to Burnett order. *J. Fluid Mech.* **361**, 41.

Shukla, P. & Alam, M. 2008 Nonlinear stability of granular shear flow: Landau equation, shearbanding and universality. In *Proceedings of the International Conference on Theoretical and Applied Mechanics* (ISBN 978-0-9805142-0-9), 24–29 August, Adelaide, Australia.

Shukla, P. & Alam, M. 2009 Landau-type order parameter equation for shearbanding in granular Couette flow. *Phys. Rev. Lett.* **103**, 068001.

Shukla, P. & Alam, M. 2010 Nonlinear stability and patterns in two-dimensional granular plane Couette flow: Hopf and pitchfork bifurcations, and evidence for resonance. *J. Fluid Mech.* (submitted).

Stewartson, K. & Stuart, J. T. 1971 A non-linear instability theory for a wave system in plane Poiseuille flow. *J. Fluid Mech.* **48**, 529.

Stuart, J. T. 1960 On the nonlinear mechanics of wave disturbances in stable and unstable parallel flows. *J. Fluid Mech.* **9**, 353.

Tan, M.-L. 1995 Microstructure and macrostructure in rapid granular shear flow. PhD thesis, Princeton University, USA.

Tan, M.-L. & Goldhirsch, I. 1997 Intercluster interactions in rapid granular shear flows. *Phys. Fluids* **9**, 856.

Tsimring, L. S. & Aranson, I. S. 1997 Localized and cellular patterns in a vibrated granular layer. *Phys. Rev. Lett.* **79**, 213.

Umbanhower, P., Melo, F. & Swinney, H. L. 1996 Oscillons in vibrated granular media. *Nature* **382**, 793.

Watson, J. 1960 On the nonlinear mechanics of wave disturbances in stable and unstable parallel flows. *J. Fluid Mech.* **9**, 371.